SANDIA REPORT

SAND2015-4431
Unlimited Release
Printed June 2015

Advanced Imaging Optics Utilizing Wavefront Coding

David A. Scrymgeour, Kathleen Adelsberger, Rob Boye

Prepared by
Sandia National Laboratories
Albuquerque, New Mexico 87185 and Livermore, California 94550

Sandia National Laboratories is a multi-program laboratory managed and operated by Sandia Corporation, a wholly owned subsidiary of Lockheed Martin Corporation, for the U.S. Department of Energy's National Nuclear Security Administration under contract DE-AC04-94AL85000.

Issued by Sandia National Laboratories, operated for the United States Department of Energy by Sandia Corporation.

Available to DOE and DOE contractors from
U.S. Department of Energy
Office of Scientific and Technical Information
P.O. Box 62
Oak Ridge, TN 37831

Telephone: (865) 576-8401
Facsimile: (865) 576-5728
E-Mail: reports@adonis.osti.gov
Online ordering: http://www.osti.gov/bridge

Available to the public from
U.S. Department of Commerce
National Technical Information Service
5285 Port Royal Rd.
Springfield, VA 22161

Telephone: (800) 553-6847
Facsimile: (703) 605-6900
E-Mail: orders@ntis.fedworld.gov
Online order: http://www.ntis.gov/help/ordermethods.asp?loc=7-4-0#online

SAND2015-4431
Unlimited Release
Printed June 2015

Advanced Imaging Optics Utilizing Wavefront Coding

David A. Scrymgeour, Kathleen Adelsberger*, Rob Boye
Department Names
Sandia National Laboratories
P.O. Box 5800
Albuquerque, New Mexico 87185-MS1082

*Currently at Corning, Inc.
Rochester, NY

Abstract

Image processing offers a potential to simplify an optical system by shifting some of the imaging burden from lenses to the more cost effective electronics. Wavefront coding using a cubic phase plate combined with image processing can extend the system's depth of focus, reducing many of the focus-related aberrations as well as material related chromatic aberrations. However, the optimal design process and physical limitations of wavefront coding systems with respect to first-order optical parameters and noise are not well documented. We examined image quality of simulated and experimental wavefront coded images before and after reconstruction in the presence of noise. Challenges in the implementation of cubic phase in an optical system are discussed. In particular, we found that limitations must be placed on system noise, aperture, field of view and bandwidth to develop a robust wavefront coded system.

ACKNOWLEDGMENTS

This work was funded under LDRD Project Number158755 and Title "Advanced Imaging Optics Utilizing Wavefront Coding".

Substantial portions of this report were adapted from Kathleen Adelsberger's dissertation at the University of Rochester. She performed the experimental work and developed the models while here at Sandia as a student intern.

CONTENTS

FIGURES

NOMENCLATURE

SNL	Sandia National Laboratories
PSF	Point spread function
OTF	Optical transfer function
FFT	Fast Fourier transform
CMM	Coordinate measuring machine
WLI	White light interferometry
SNR	Signal to noise
MTF	Modulation transfer function

1. INTRODUCTION

Imaging systems have followed a rapid shift to digital detection over the past few decades, but the optical design process has been slow to follow. Optical system design is still largely approached as a set of independent design steps, with the lenses, detection and electronics all optimized as separate entities. We examine a systematic approach to optimization for the specific case of cubic phase wavefront coding, where the optics are designed in conjunction with object spectral bandwidth, actual detector properties and an image processing algorithm to develop a final image. In this work, we initially investigate the methods common to wavefront coding based on the introduction of a phase plate at the pupil. The desired result of wavefront coding optics is an invariantly blurred point spread function (PSF) throughout the field in the image plane, which is corrected using digital signal processing. The PSF also remains invariant through an extended depth of focus, alleviating the effect of aberrations, such as field curvature and axial chromatic, which cause a variation in focal position with field or wavelength, respectively.

Wavefront coding, and computational imaging in general, follows the idea of shifting some of the traditional optical burden onto the electronics and computer processing. The benefit to this approach is that electronics and processing capabilities are reconfigurable, cheap, weigh very little, and take up a smaller space in comparison with optics. The designs of most optical systems are driven by one of these limitations, so it is easy to understand the potential benefit offered by such a hybrid electro-optical system. Electronic processing, however, does come with its disadvantages, some of which will be examined in this work. In particular, noise often becomes a problem in a system which employs digital image processing. Understanding the tradeoff between system size, complexity, and performance of a system with wavefront coding will assist the early lens design process.

Lens designers make tradeoffs early in the design process that determine the layout of the final system. In a traditionally designed optical system, where optics and electronics are designed separately, the electronic parameters typically have a minimal impact on the first-order optical design. At most, designers consider the electronic pixel size to help determine the resolution or sampling requirement. Jointly optimized electro-optical systems, on the other hand, require a much more detailed knowledge of the system requirements and capabilities even while laying out the first-order parameters. Here, we investigated the relationship between optical and electronic parameters in a wavefront coded system. We summarized the conclusions into a set of design parameters to guide lens designers who wish to include wavefront coding in an optical system. We developed guidelines with respect to system aperture ranges which will benefit from wavefront coding, initial noise levels that will tolerate image processing, and how these parameters may impact the ideal amount of phase to add. These guidelines were verified with simulations and validated experimentally.

2. BACKGROUND - WAVEFRONT CODING AND COMPUTATION IMAGING

Departing from the traditional design process, beam encoding techniques have been established to increase the system depth of field or otherwise improve system performance.[1] A beam encoding system is one in which the wavefront is encoded with a designed phase to engineer the image point spread function in a known way. Beam encoding methods fall into two categories: smooth coding using a continuous phase surface, and discrete coding using a discontinuous surface such as a diffuser or binary mask. The encoded phase is designed in conjunction with an image processing algorithm, which decodes the information collected by the detector to create the final image. We use the term ”wavefront coding” to describe smooth phase contributions added in the pupil. ”Beam encoding” is a more general term encompassing all methods of altering the phase of an optical system, even in a discontinuous manner, in conjunction with image processing. Many beam encoding systems are designed to increase the depth of field of the system as an alternative to the mechanically moving parts in a variable focus system. For example, the logarithmic asphere provides extended depth of field imaging by adding a phase plate that imparts spherical aberration on the beam.[2, 3] Other examples are the annular axicon and light sword optical elements, both of which extend depth of focus by spreading light into a focal line along the optical axis.[4] Ashok and Neifeld approach discontinuous beam encoding from a similar electronic imaging standpoint employing a pseudo-random phase mask in the pupil plane to achieve superresolution.[5]

Groups exploring wavefront coding employ aspheric elements or additional phase plates in the pupil to engineer the point spread function (PSF), such that the optical transfer function (OTF) has particular properties over the image that enable image reconstruction through post processing.[6-12] This engineered PSF in wavefront coding has the same shape throughout the image field, i.e. the system must be designed to have a much larger isoplanatic region than without wavefront coding, and is subsequently accounted for using digital signal processing. Beam encoding systems have also been developed for a range of other purposes. Stork and Robinson introduced the idea of adding the image processing capabilities to the optical design process.[13] Their work is instrumental in mapping out an optimization method that includes an end-to-end merit function consisting of both the optical and electronic processing systems. Ng and Levoy use a technique closely related to wavefront coding, where a lenslet array maps the pupil onto the detector.[14] This method retains directional information from the rays, and combined with an image processing algorithm, the system allows for digital refocusing of a captured image. A similar method places an amplitude attenuating mask near the image plane to recover the four-dimensional light field, like Ng and Levoy, but without requiring a lenslet array.[15] Lee et al. demonstrate a system designed using the theory behind wavefront coding to engineer the point spread function without any additional phase surfaces.[16] Instead, they use a number of aspheric surfaces to achieve the desired PSF. Finally, an interesting corollary to the cubic phase plate is the Airy beam, which produces an intensity pattern along the beam nearly identical to the cubic phase PSF.[17]

Many of these groups have approached the idea of wavefront coding from a theoretical and ideal standpoint. In some cases, extensive theory and simulation results are presented but are not validated with an experimental setup.[18] Groups that included experimental data or physical systems made an effort to diminish nominal system noise [10], worked only with monochromatic illumination or required specific system parameters, like object distance, to be tightly controlled and accurately known.[19] Arnison et al. implemented wavefront coding in a high-aperture microscope objective; however, their system required only a small amount of cubic phase and a low level of system noise.[20] These groups demonstrated the capabilities of wavefront coding and a corresponding image reconstruction algorithm on an optical system under ideal circumstances.

Alternately, we approached this problem from an optical design perspective. We explored the design space by varying different parameters to judge their impact on the effectiveness of the added cubic phase and reconstruction. We took into account aspects of a physical system that are often ignored, such as noise and alignment errors, and described the implications this information has on the final system. From the results of our analysis, we developed a set of design guidelines and map out the design space where wavefront coding is likely to be effective. While our work here only considers cubic phase wavefront coding, the design approach is applicable to other wavefront coding systems.

3. SIMULATIONS

In this chapter, we define the optical system and image processing model, including the assumptions made and the guidelines used in performing our analysis. We discuss the sampling relationships required between the image and pupil planes, including how this pertains to our deconvolution metric. We examine the bandwidths and spectral weighting used in our simulations. Next the cubic phase plate is described. We also introduce our optical system objects, image processing algorithm and a corresponding spatial frequency response technique used to calculate the one dimensional MTF. Finally, we discuss the image evaluation metrics used to determine reconstructed image quality.

3.1 Assumptions

A few general assumptions were made throughout the work in this work. We assumed all illumination, both in theoretical models and experiments, was temporally and spatially incoherent. We anticipate that the application of this work is best suited to systems that image diffusely scattered incoherent light or thermal based extended sources. The illumination in these cases is highly incoherent, and our assumption is appropriate.

We also assumed a Gaussian noise model when noise is included in our simulations. We will discuss contributions from noise sources that do not follow a Gaussian curve, such as shot noise, which is represented by Poisson statistics. However, in these cases, we assumed that either the noise contribution is large enough that the Poisson curve can be approximated by a Gaussian, or that the non-Gaussian noise contribution is negligible.

Other specific assumptions were made which pertain to only a portion of the work. These assumptions are discussed within the section to which they pertain.

3.2 Theory

The goal of wavefront coding in the pupil is to engineer the optical transfer function of a system in a deliberate manner, such that it is known and is similar throughout a desired reconstruction range. This reconstruction range is manifested as an extended depth of focus when a cubic is chosen as the phase function. The cubic phase method is commonly used to increase the range of in-focus objects in a scene.[6] However, an extended depth of focus is also helpful in correcting defocus related aberrations.[7] The effect of wavelength on focal length, defined as axial chromatic aberration, was discussed in detail in Section 1.2. Likewise, Petzval field curvature is a variation in focus with respect to field. The in-focus points of a system with non-zero Petzval curvature form a curved surface instead of a plane, resulting in field-dependent blur in systems with a flat image plane. Astigmatism is yet another focus dependent aberration, where sagittal and tangential rays from the pupil come to focus at different positions along the axis. In all of these cases, if the wavefront coding and reconstruction algorithm is able to extend the depth of focus so that it encompasses the entire range of in-focus points, these aberrations will no longer contribute to image blur. For the purpose of this work, we choose to focus on using cubic phase for the correction of axial chromatic aberration.

3.3 General Model

Our optical system simulations were based upon a model that incorporated the lens design software, Zemax, with Matlab processing capabilities. The overall structure of the model remained the same throughout each of the different systems that we developed. The lens prescription, comprising a simple imaging lens or lenses and an additional phase element, for each system that we modeled was entered into Zemax. In the optical model, we also specified a set of system parameters including aperture, wavelength and field of view. Two-dimensional point spread functions (PSFs) and one-dimensional modulation transfer functions (MTFs) were captured from Zemax for each system both with and without wavefront coding phase optics present. This created a set of data for the nominal (traditional) system and a second set of data for the phase encoded system. The PSF contained information regarding the aberrations present in the system. MTFs are generally better suited as a measure of system performance rather than a system diagnostic tool. We will discuss these system performance metrics later.

The next step was to import the PSFs into Matlab and set up our optical system parameters within Matlab using the parameters from Zemax. The sampling relationships between the pupil and image planes, discussed in detail later in Section 3.4, were calculated according to the image pixel size used in creating the PSF. Other system parameters, such as focal length, wavelength range, and field of view were copied from the Zemax system data.

An ideal object was next loaded into our simulation. Objects imaged for different purposes included a greyscale scene, resolution target, or grid depending on our desired output and visualization. The object was convolved with the PSF at discrete wavelengths within the broadband range to create a series of blurry images. A continuous illumination spectrum is not easily modeled; instead, discrete wavelengths were chosen which were spread approximately evenly in frequency throughout a wavelength range and were scaled according to our desired spectrum. These wavelengths were averaged, with their respective weights, to simulate a broadband spectrum. Next, a single-wavelength PSF was chosen as the deconvolution kernel, and the deconvolution algorithm was applied using this kernel. When a grid was chosen as the object, an edge from the reconstructed image can be processed using the Spatial Frequency Response Matlab program (sfrmat) to determine the MTF of the final reconstructed image.

3.4 Sampling

Highly important to the simulated optical system model is understanding the sampling relationship between the pupil and image planes. To ensure that simulations run efficiently and correctly, the number of pixels in both planes must be equivalent. For the purposes of this work, we assumed square pixels within square arrays. The number of pixels along one dimension of the array (equivalent in both the pupil and image planes) is given by N_x. The size of the pixels was generally not consistent between the two planes; however, the relationship of physical array width and pixel size must obey the following relationships:

$$dx = \frac{\lambda z}{h}$$

$$du = \frac{\lambda z}{S}$$

$$S = N_x dx \geq 2CA.$$

Equation 1

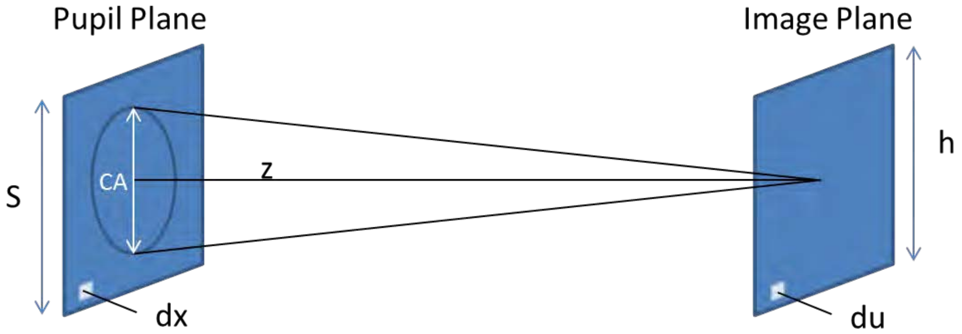

Figure 1: Important parameters are labeled on this figure showing the exit pupil plan and image plane of an optical system.

Figure 1 illustrates the optical system parameters that establish these sampling relationships. λ represents the system design wavelength, z refers to the distance between the pupil plane and image plane, while dx and du represent pixels sizes in the pupil and image planes, respectively. The width of the square image plane is described by h. S is the parameter that describes the physical size of the pupil plane array, not the size of the exit pupil. In fact, S must be at least twice the size of the physical exit pupil, described by CA, to ensure no aliasing is introduced to the simulated images.

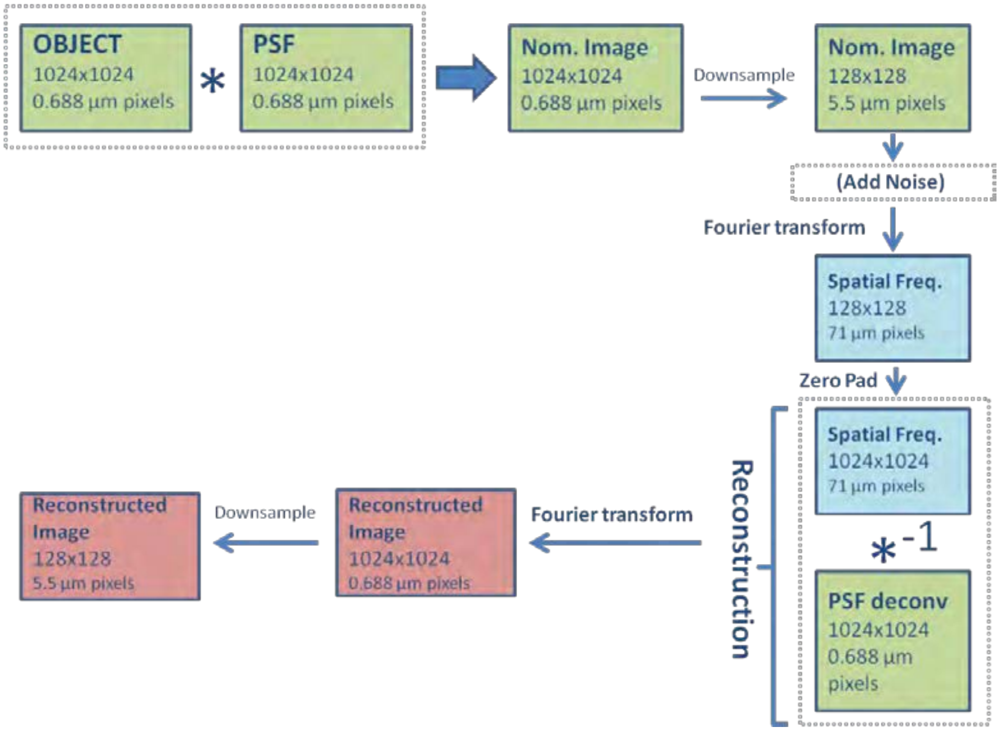

Figure 2: Diagram of MATLAB code showing the sampling and pixel size of each parameter. Images must be down sampled to reflect the physical pixel size of the detector.

Along with correct sampling relationships, the physical size of the detector pixels must also be modeled accurately to ensure realistic results. The physical extent of a pixel determines the smallest system resolution. Two point spread functions separated by a distance smaller than the pixel width are not resolvable by the detector; they appear as originating from the same point. The sampling of the detector, inversely related to the physical size of the pixels, must be greater than the Nyquist limit of the optical system in order to prevent aliasing in the image. Nyquist sampling occurs when the sample spacing is half the distance of the highest frequency signal incident upon the detector.[21]

Figure 2 displays a schematic of the MATLAB code used to simulate our optical system. The diagram details the sampling used at each step of the simulation. Beginning with an ideal object and imported Zemax PSF, both sampled with 0.688 µm pixels, the two arrays were convolved to simulate the highly sampled image. This image was then down sampled by a factor of eight, resulting in 5.5 µm pixels, to simulate the image captured by our experimental detector. When performing a noisy simulation, noise was added to the image at this point. Next, the Fourier transform was taken to move to the spatial frequency domain. The frequency domain image was zero-padded to increase the array back to the original size of 1024x1024. This method of zero-padding involves no interpolation, so information was not artificially altered. From this point, we took the highly sampled deconvolution PSF and deconvolved it from the zero-padded Fourier transform of our image. The diagram labels the deconvolution process simply as ”Reconstruction,” but in reality, a few different deconvolution metrics were included and analyzed here. Finally, the reconstructed image was created by taking the Fourier transform of the reconstructed spatial frequencies. When comparing final reconstructed images with experimental images, we down sampled one last time to make sure both images were sampled using the experimental 5.5 µm pixel size.

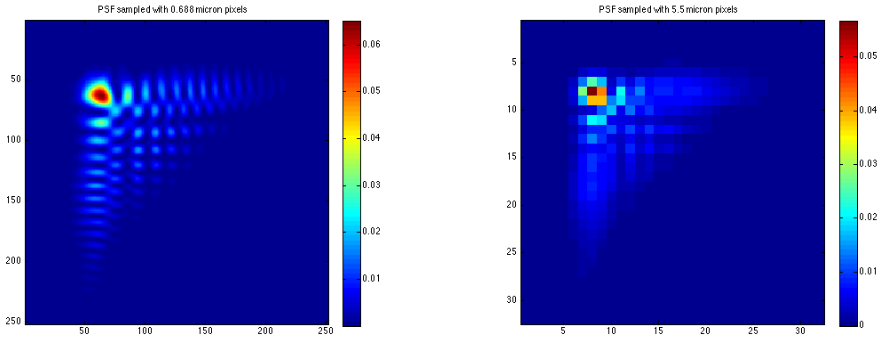

(a) 0.688 µm pixel size (b) 5.5 µm pixel size

Figure 3: The same PSF, created using 500 nm illumination from a wavefront coded doublet system, is sampled with two different pixel sizes.

The reason we chose not to perform all calculations using arrays sampled at the larger 5.5 µm pixels lies in the small features of the PSF, which cannot be adequately sampled with large pixels. The PSF in Figure 3a, from a simulated wavefront coded doublet system, is sampled with pixels smaller than 1 µm in size resulting in over 150 pixels along its width. This sampling provides enough detail to resolve the fine features in the PSF. In comparison, the PSF in Figure 3b is sampled with pixels eight times larger; the actual pixel size here is on the small end of what is commercially available and matches our experimental detector. The entire width of the PSF spans about 20 pixels on the experimental detector, while many of the fine features extend across only one pixel. Sub-pixel shifts of this PSF would result in significantly varying images. Using a simulated deconvolution PSF with higher sampling eliminated this problem.

3.5 Bandwidths

We modeled and compared results from three different bandwidths in our simulation, shown in Figure 4. For each bandwidth, we chose a series of discrete wavelengths, which were evaluated individually then weighted to produce a single broadband image. Two important applications of wavefront coding are ground based and satellite imaging systems of objects illuminated by sunlight. For this reason, we chose our spectrum based on the ASTM G173-03 Reference Spectra Global Tilt, which includes spectral radiation from the solar disk plus diffuse reflection from the sky and ground, to simulate light that would be captured on the earth’s surface. We multiplied these values by the quantum efficiency of the Kodak KAI-08050 silicon CCD. This assumption is a good approximation of the spectrum seen by a typical silicon detector imaging an object illuminated by sunlight on the earth’s surface.

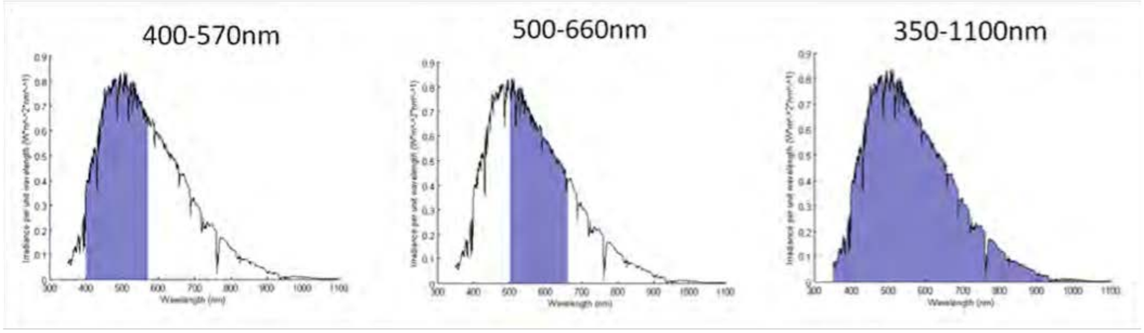

Figure 4: We model three different bandwidths in our simulation. Midband widths include 400-570nm (left), and 500-660nm (middle) to determine if the optimal cubic phase has a dependency on the average wavelength of the band. The large bandwidth extends from 350nm to 1100nm (right).

We were interested in the dependency of optimal cubic phase on both the bandwidth size and average wavelength of the broadband region chosen. Consequently, we modeled two mid-width wavelength ranges (400-570nm and 500-660nm), and one large bandwidth range (350-1100nm). The spectra of these bandwidths are shown in Figure 4. We initially also included an analysis of smaller bandwidths of 30nm but concluded that the nominal system already performed near the diffraction limit, rendering wavefront coding unnecessary for chromatic correction.

3.6 Phase Surface

We added a cubic phase surface to the pupil of our imaging system to directly modify the wavefront and, in turn, the point spread function. The phase surface that we used for our noiseless simulations was the cubic phase employed by Cathey and Dowski.[1] In our Zemax model, the phase was described by an extended polynomial following the function

$$\Theta(X,Y) = \alpha(X^3 + Y^3),$$

Equation 2

where X and Y are normalized pupil coordinates, and α is a constant that determines the amount of phase added in the pupil. Figure 5 shows a map of the surface sag of this ideal cubic phase.

When the added phase was chosen carefully, the discrete-wavelength MTFs of the entire wavelength band followed a more similar shape. However, this added phase also caused the MTF contrast to decrease. If the MTF contrast fell to zero or dropped below the noise floor, these spatial frequencies were no longer recoverable using an inverse filter. Examples of nominal and wavefront coded MTFs are displayed in Figure 6. In this figure, a singlet system was focused for diffraction-limited performance at 500 nm. The MTFs shown are at 660nm; as expected, the predominant aberration in the nominal system MTF, shown on the left, is defocus. Zeros occur in the nominal MTF very close to the center point meaning that spatial frequencies beyond this value are lost at this wavelength. The wavefront coded MTF, on the right, pushes out the zeros much farther away from the center point, allowing more information to pass to the image plane.

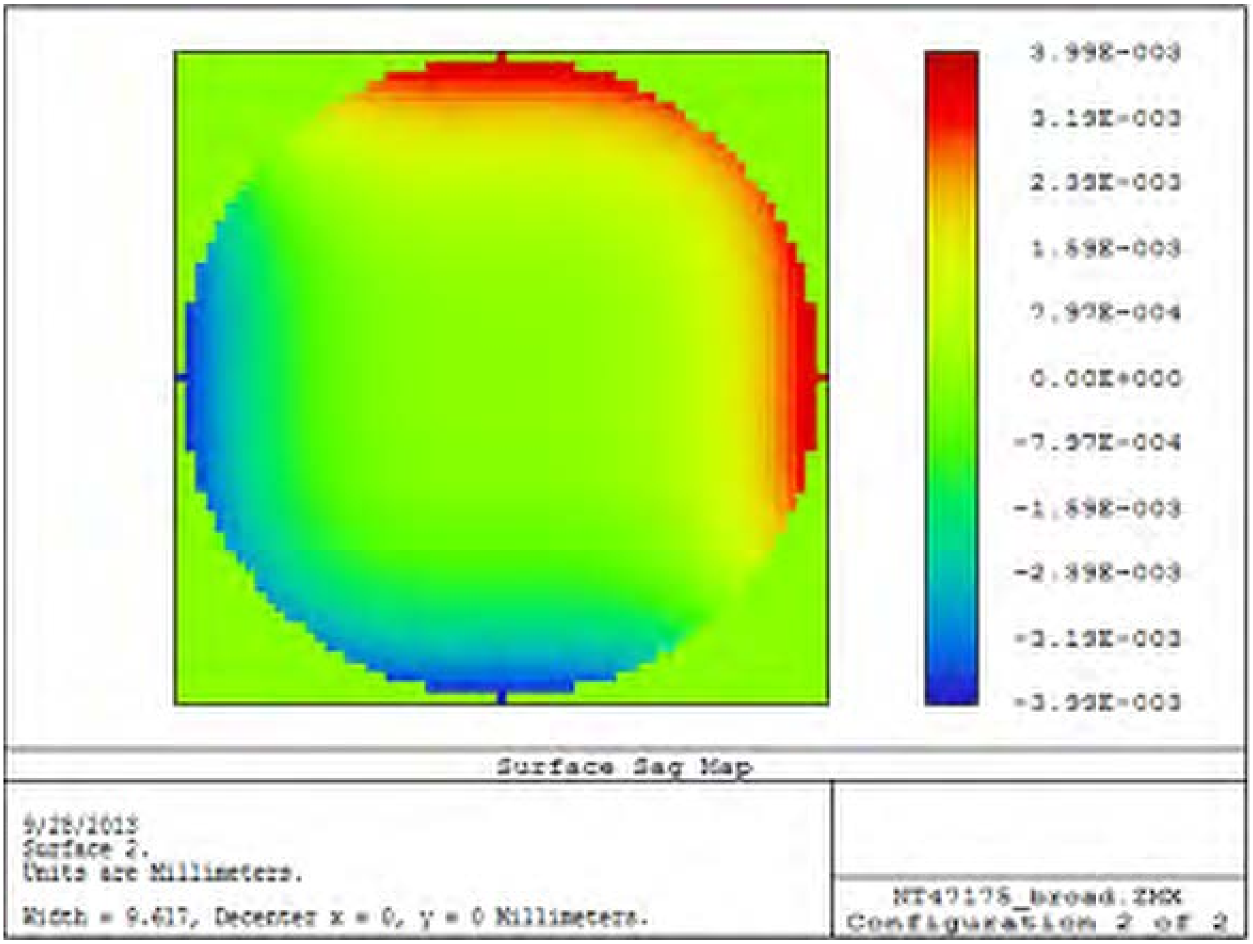

Figure 5: Surface sag of ideal cubic phase with α = 70μm over a clear aperture of about 10mm.

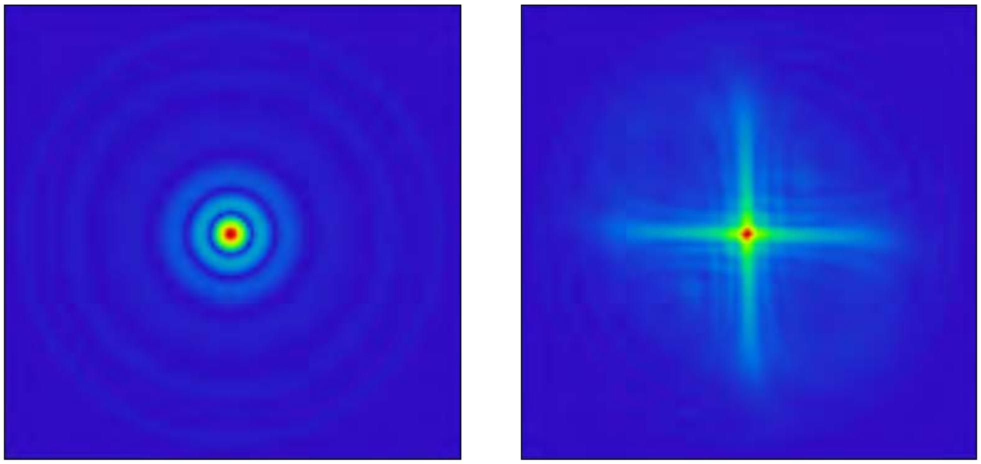

Figure 6: Shown are two-dimensional MTFs of a singlet lens with 660 nm illumination. Left is the nominal system showing a significant amount of defocus and clear rings of zero contrast. Right is the same system with added cubic phase in the pupil. The region where modulation goes to zero is farther from the center allowing for higher spatial frequencies to pass through the system.

Similarly, in noisy systems (discussed in the next chapter), any low contrast values of MTF, near but not necessarily equal to zero, are indistinguishable during recovery. Optimization of the value of added phase becomes a balancing act between making the MTF curves similar throughout the wavelength band, while retaining a high enough contrast that the signal does not reach zero and become indistinguishable from the noise. Based upon this analysis, the optimization of the phase surface becomes a different problem when noise is added to the simulation, and is thus discussed in greater detail in the next chapter.

3.7 Image Processing Algorithm

We discuss the development of an image processing algorithm to use with each recorded image based upon an understanding of the physical optics characteristics of our system.[22] The recorded image of an optical system can be represented as a convolution of an object, f and a point spread function, h as follows:

$$g = f * h.$$

Equation 3

In Fourier space, the relationship becomes

$$G = FH,$$

Equation 4

with G, F, and H representing the respective Fourier transforms of g, f, and h. H is also called the optical transfer function (OTF). The image, then, is an inverse Fourier transform of G,

$$g = \mathcal{F}^{-1}\{FH\},$$

Equation 5

and exact recovery of the object can be done by a simple deconvolution or in Fourier space by a division,

$$f = \mathcal{F}^{-1}\left\{\frac{G}{H}\right\},$$

Equation 6

However, as discussed earlier, images detected using physical systems contain a noise contribution, n, as follows:

$$g = \{f * h\} + n.$$

Equation 7

Typically only the statistics of the noise function are known, not the exact function itself, so the noise contribution makes exact recovery of the object impossible. The goal, then, becomes recovering an image that is as close as possible to the original object while reducing the effect of noise on the final image.

The ideal inverse filter involves dividing the Fourier transform of the deconvolution kernel, described by the OTF, from the Fourier transform of the wavefront coded image, per equation 2.8. This straight division creates a few mathematical problems when the system OTF and deconvolution OTF do not match exactly.

Because the ideal inverse filter requires dividing by the OTF, any zero values within the OTF will cause infinitely high values in the reconstructed image. To mitigate this problem, we employed a threshold to the OTF in our simulation. All values below the arbitrary threshold are set to non-zero nominal value, while all other values remain the same. In the absence of noise, the wavefront coded OTF by design should not have values below this threshold up to a spatial frequency cutoff. However, when we introduce noise to our simulation, individual pixel values may very well fall below this threshold, and unaltered, would produce undesirable spikes in the recovered MTF.

Figure 7: Original (perfect) object is shown on the left, and image on the right is reconstructed using an ideal inverse filter. Diagonal banding is evident throughout the image.

Images created using a simple inverse OTF deconvolution filter typically have a pronounced banding pattern in the reconstructed image. Figure 7 shows an example of this effect in the deconvolved image on the right. This banding arises from two side lobes at a positive and negative diagonal spatial frequency in the OTF. Smoothing the inverse filter by convolving with a carefully sized NxN square kernel is an effective way to reduce this banding effect. Smoothing with a kernel too large reduces the effectiveness of the deconvolution, while a kernel too small fails to remove the banding effect. In most cases, an 11x11 pixel kernel was adequately sized to remove banding while not significantly reducing resolution in the reconstructed image.

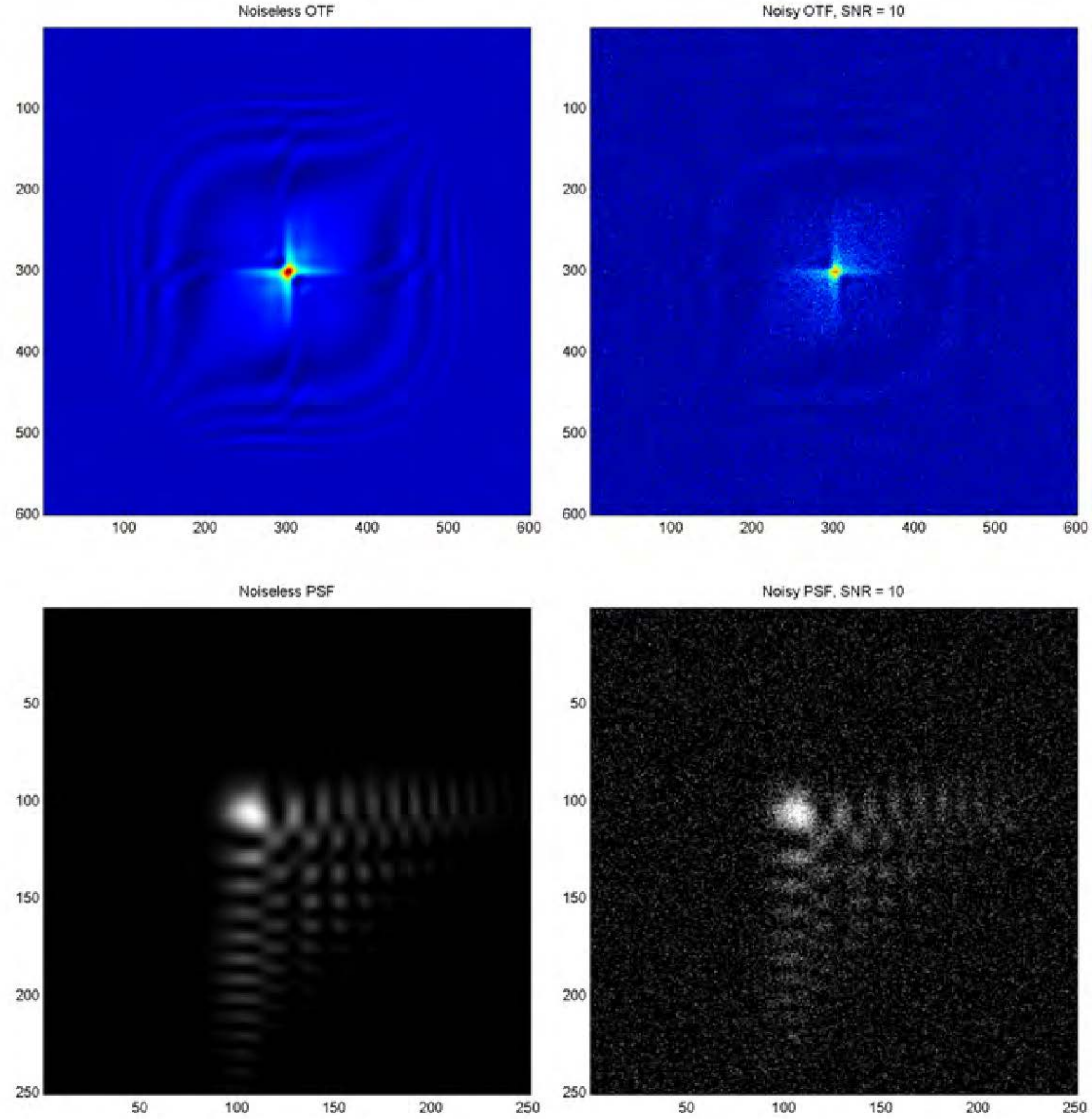

Figure 8: This image series shows the effect of noise on the OTF and PSF. Leftmost images show a noiseless OTF (top) and PSF (bottom) for a broadband system with WFC = 70 μm. Rightmost images show the effect a noisy system with a SNR = 10.

With these modifications, the ideal inverse filter can work well in systems without noise; however, the inverse filter quickly breaks down in a noisy system and ends up amplifying the noise rather than just the signal. This is shown mathematically,

$$G_{deconvolved} = \frac{G}{H} = F + \frac{N}{H}.$$

Equation 8

The noise term, *N/H*, approaches a singularity where the OTF is zero. For small *H* non-zero values of the OTF, the noise is still amplified. Noise in an optical system degrades the form of the OTF as well as the PSF, shown in Figure 8. For our noisy physical system, we sought a more robust deconvolution algorithm.

3.8 Image Analysis

Images can be analyzed in a number of ways, often corresponding to the application and the image features that are most relevant to the application. We chose to focus mainly on image information content, measured by the modulation transfer function.

The MTF can be calculated from the PSF alone because of the Fourier transform relationship between the two quantities. Optical simulations provide PSFs with sufficient sampling to construct the MTF. Extracting the PSF experimentally, however, is very challenging because the pixel size required to adequately sample the PSF is smaller than what is now readily accessible. This problem was discussed previously in Section 3.4, and Figure 3 highlights this problem. One potential solution to this sampling problem, magnifying the PSF using additional optics, overcomes detector array limitations but complicates the system with alignment and relay aberration artifacts.

Instead, we use the same MTF method to extract the one-dimensional MTF for both the simulation work presented here as well as experimental validation. To this end we adopt the slant-edge spatial frequency response (SFR) from the ISO-12233 standard via the MATLAB function sfrmat3.[23, 24] The SFR requires a black-to-white slanted edge object as input, shown in Figure 9. The algorithm then fits a best-fit line to the slanted edge, supersamples this fit line, and then calculates the one-dimensional line spread function of the fit line. Taking the discrete Fourier transform of the line spread function results in the reported SFR.[25] The MTF curves displayed in the results sections are the normalized modulation of this Fourier transform.

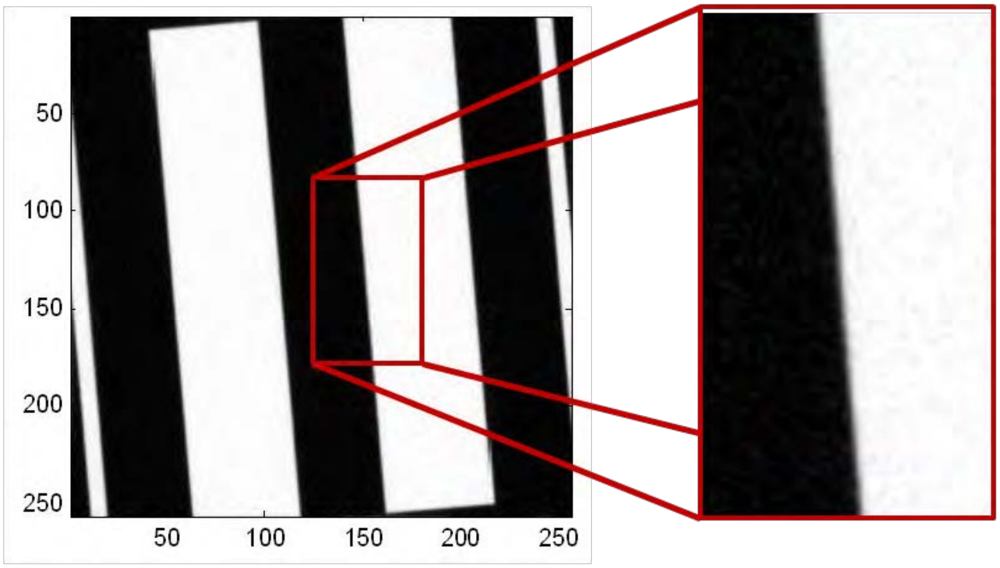

Figure 9: The object used for most of our simulations is a sequence of black and white bars, angled at about 5 degrees from vertical. A subset of the image is selected to contain a single black to white transition for use with the spatial frequency response algorithm.

We selected one black-to-white edge from each simulated image as our region of interest for any MTF calculations. We found consistent results from a region of interest located in the center of the image and located toward the edge of the image, since our field-of-view was smaller than the isoplanatic image patch. Some reconstructed images, however, contained edge artifacts that extended around the border of the image. These edge artifacts could have been minimized by including a grey buffer around the image edge and careful algorithm design. Instead, we simply chose to use a region of interest near the center of the image for analysis purposes. The one-dimensional MTF was then extracted using the SFR algorithm, described previously. The resulting MTF curves gave us a few important conclusions about the information content of the nominal and reconstructed images. The 1-D MTF mapped the image contrast for each spatial frequency and allowed us to determine the nominal spatial frequency cutoff, above which information is lost and cannot be recovered. We also deduced the spatial frequency range over which contrast was boosted by the deconvolution algorithm and were able to determine if noise became a limiting factor.

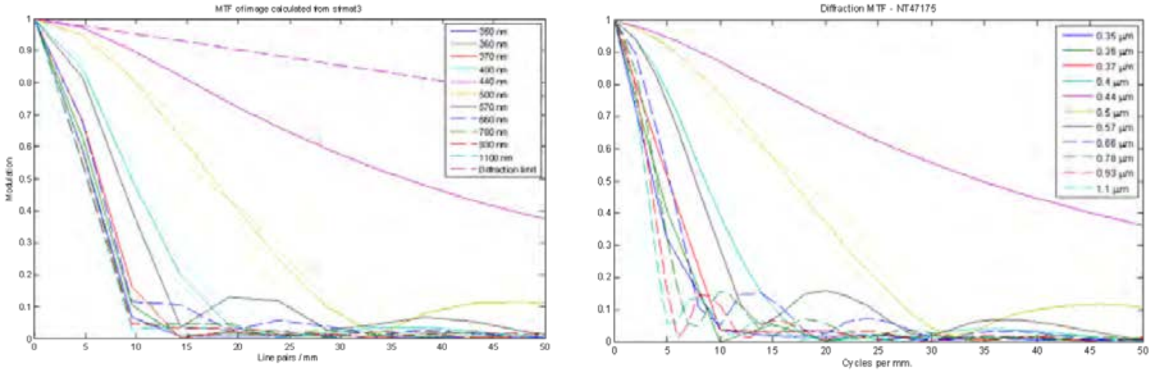

Figure 10: Left curves are produced by the SFR algorithm, while right curves are direct output from Zemax. A comparison shows good agreement greater than 10 lp/mm, but disagreement below this frequency. The SFR algorithm interpolates data between measurement points based on the number of pixels included in the slanted line selection. More pixels included in this selection allow for better sampling of these curves; the selection area is limited by the size of the rectangle that can be superimposed on the grid image.

We include a comparison of the SFR algorithm results with a series of MTF curves exported from the Zemax model of a nominal (zero added phase) singlet. In our comparison, Zemax curves were generated for each of a set of discrete wavelengths. Grid images were also simulated in Matlab by convolving the PSF of each wavelength with the grid object. The SFR algorithm was then applied to the slanted line selection to generate MTF curves. Results are shown in Figure 10.

4. SIMULATION RESULTS

In this chapter, we analyze a series of simulations in both the absence of noise and added noise. We began to develop our wavefront coding simulation in systems that were assumed to be noise-free. We initially made this assumption for two reasons. First of all, noiseless systems were easier to characterize and validate to ensure the optical system model and image processing algorithm were performing as expected. Secondly, we wished to characterize the impact of different forms of noise within a system and initially needed to establish a baseline noiseless system with which to compare our results. Traditionally, most optical systems are designed without considering noise effects until after a design form is determined. Understanding first how the system parameters and final image are affected by the addition of phase to the pupil and subsequent reconstruction without noise allowed us to determine the effect of the phase on system performance and to what degree including noise in the first-order design would assist in the design process.

4.1 Noiseless System Simulation and Results

4.1.1 Background

A theoretical comparison of axial chromatic aberration in both the experimental singlet and doublet lenses is shown in Figure 11. To create this plot, the best focus was determined using a Zemax simulation, and the departure from best focus at 500 nm is plotted. The dashed black lines represent the approximate limits of near diffraction-limited resolution; a defocus amount within these limits enables nearly diffraction-limited system performance, while performance degrades significantly when defocus is outside these limits. The criteria for determining these approximate limits involved an MTF curve that did not fall to zero contrast at a spatial frequency smaller than the diffraction-limited cutoff and retained at least half the value of the diffraction-limited contrast for all frequencies below cutoff. The wavelength range of nearly diffraction-limited performance for a singlet, then, is between 470 and 520 nm, whereas the doublet achieves this same performance for a wavelength range from below 350 nm to 570 nm. We can later compare the reconstructed performance of a wavefront coded singlet with this figure to determine the additional benefit provided by the image processing.

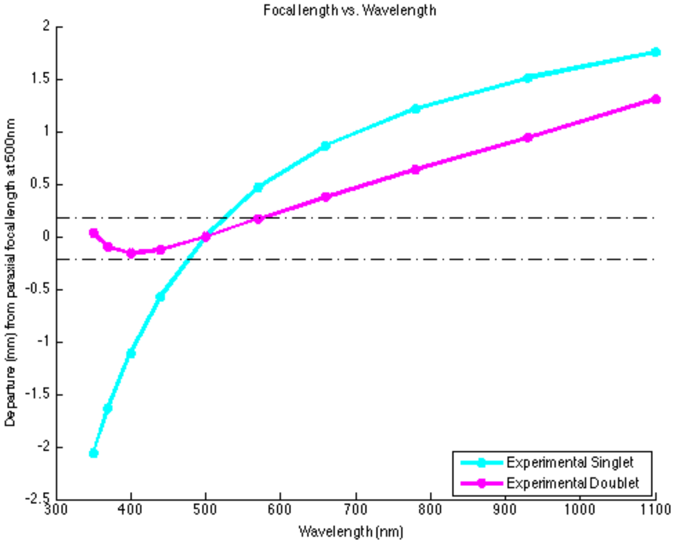

Figure 11: Variations in focus versus wavelength are shown for both the experimental singlet and doublet systems at F/10 for a 100 mm focal length. The plots show the departure from best focus at 500 nm for a range of wavelengths. The region between the

dashed lines indicates the focal positions that result in nearly diffraction-limited performance.

4.1.2 Optimal Phase vs. Bandwidth

We are interested now in investigating how the illumination bandwidth directly impacts the optimal system design when using cubic phase wavefront coding. Analyzing the MTF curves at a series of individual wavelengths for a nominal singlet, included in the leftmost plot in Figure 12, clearly shows the effect of axial chromatic aberration. Wavelengths near the design wavelength, 480nm and 500nm in the figure, show nearly diffraction limited performance, while the performance for other wavelengths degrades quickly. When cubic phase is introduced to the pupil, however, the MTF curves begin to take on a similar shape. As the amount of cubic phase in increased, the curves for each wavelength become nearly identical, but the overall contrast is depressed. MTF curves for two different phase amounts are also included in Figure 12.

As discussed earlier, the additional cubic phase depresses the unprocessed curve throughout the range of spatial frequencies as compared with the nominal system evaluated at the design wavelength without the cubic-phase element. However, at wavelengths away from the design wavelength, the addition of cubic phase extends the spatial frequency of the first zero-crossing of the MTF. After processing, the reconstructed broadband MTF of the cubic phase system is clearly improved across a majority of the spatial frequency range. Note, the same image reconstruction technique can be applied to a nominal optical system (with no added cubic phase), but the zeros in the MTF for defocused wavelengths cause infinite amplification of those spatial frequencies, leaving the reconstructed image with a large amount of noise and image artifacts.

We ran a set of simulations in the absence of noise to gain insight into whether there is an optimal amount of phase to correct a particular wavelength band in a wavefront coded system and to see if this optimal phase amount changes with bandwidth. We used our Matlab model of the singlet lens and simulated images under various conditions. Figure 13 displays MTF curves for this simulated system using mid-bandwidth illumination (400-570 nm). Each subfigure represents the system with a different amount of cubic phase (from a 30 μm sag to a 200 μm sag). The red curve represents the nominal system MTF and remains constant in all six plots, as does the black curve which represents the diffraction limit. The green curve displays the wavefront coded system MTF before reconstruction; this curve becomes more depressed overall as the amount of phase increases. The blue curve represents the reconstructed MTF, after applying an adapted inverse filter as the deconvolution metric. To determine which system has the best performance, we apply two error metrics to these curves, as well as adding some of our own insight.

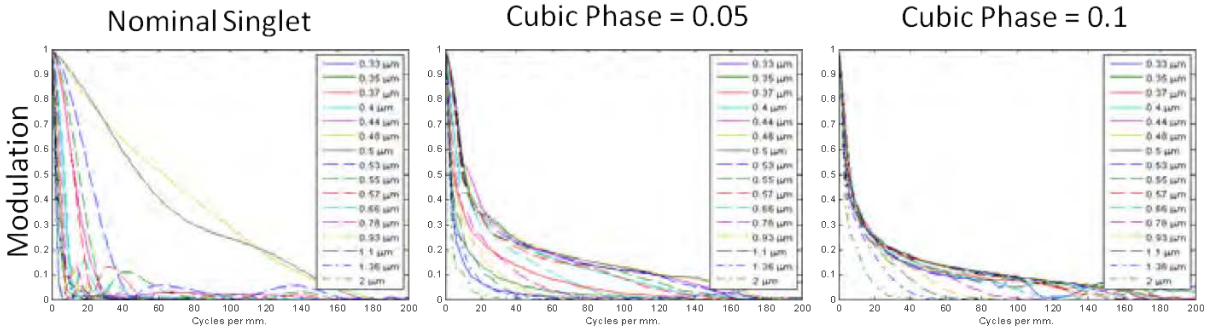

Figure 12: MTF curves are shown for a singlet with no added cubic phase (left), cubic phase with 0.05 mm sag at the edge of the clear aperture (middle), and cubic phase with 0.1mm sag (right). As cubic phase in increased, the MTF curves for each wavelength become increasingly similar to one another, but also depressed for all spatial frequencies..

Figure 14 plots the error metric values with respect to cubic phase value for three different illumination bandwidths. In both cases, the error metric values for a cubic phase of 200 µm are artificially high. Looking back at Figure 13j, we note that the green curve is no longer smooth and slowly varying like it is with lower phase amounts. Sampling of each MTF curve is approximately 1.5 lp/mm, which is determined by the size of the image subset used in the SFR analysis (displayed previously in Figure 9). Any modulation of an MTF curve at a higher rate than this sampling value will be undersampled and aliased on the MTF plot. One consequence of this high modulation with the 200 µm cubic phase system is OTF values close to zero, which amplify noise. Thus, we conclude that the blue reconstructed curve for the 200 µm cubic phase system contains amplified noise values rather than reconstructed object information. For this reason, we determined that 200 µm is too large of a phase value and we ignored these data points in our system analysis.

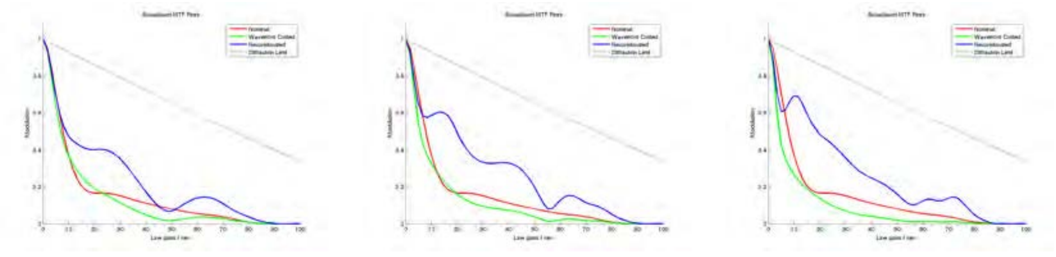

(e) 30 μm sag **(f)** 50 μm sag **(g)** 70 μm sag

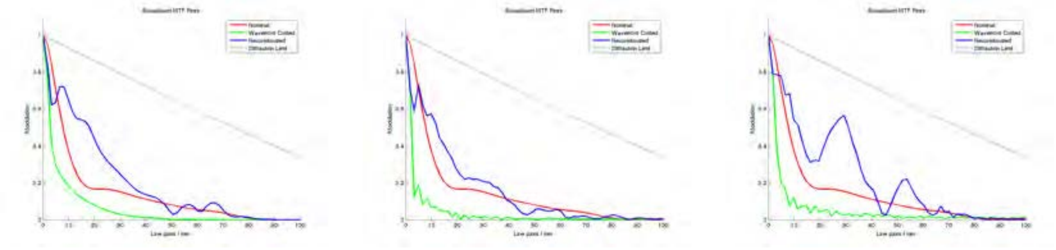

(h) 100 μm sag **(i)** 150 μm sag **(j)** 200 μm sag

Figure 13: Singlet with mid-bandwidth illumination is analyzed in a wavefront coded system with varying sag phase amounts. The jagged wavefront coded (green) curves in (i) and (j) indicate undersampling and cause artificial amplification due to noise in the reconstructed (blue) curves.

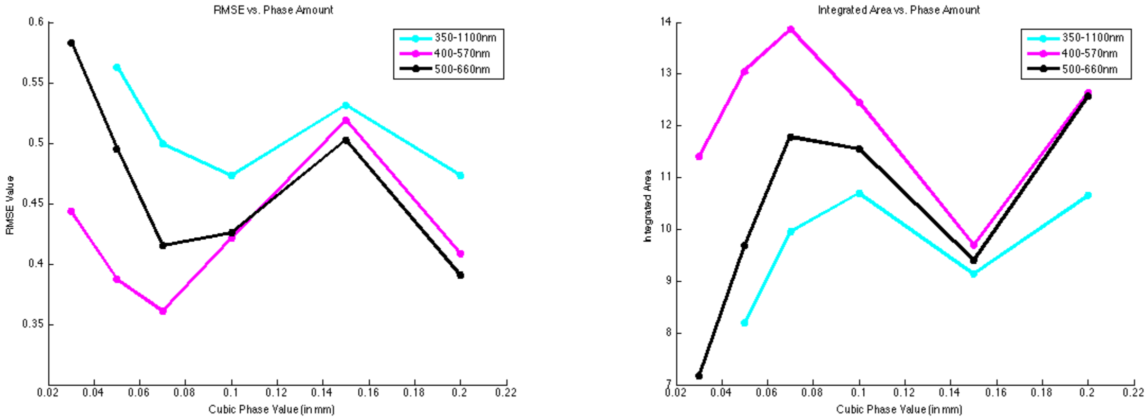

Figure 14: Three different illumination bandwidths modeled to determine optimal phase amount in a noiseless system. Discarding 200 μm phase points, optimal phase is 70μm for mid-bandwidth illumination and 100μm for wide-bandwidth illumination using both error metrics.

The rest of the data suggests a clear optimal phase value for each bandwidth. The RMSE metric, used in Figure 14a, shows a minimum error at 70 μm of cubic phase for both mid-bandwidth systems (plotted as the black and pink curves) and a minimum error at 100 μm for the wide-bandwidth system (blue curve). The integrated area metric in Figure 14b arrives at the same optimal values, this time displaying a maximum value for the highest performance systems.

4.1.3 Conclusion Noise Free Simulations

We tested the cubic phase dependency on bandwidth for three different wavelength ranges and a number of values of cubic phase. We concluded that even in the absence of noise, an optimal phase value exists for each optical system.

We also determined that the size of the bandwidth made a measurable impact on the optimal amount of phase; a larger bandwidth achieved optimal reconstructed performance with a higher amount of phase than smaller bandwidths.

In the next section, we will re-visit the optimal phase simulation with the addition of noise to the images. We expect to still find an optimal value of added cubic phase dependent on bandwidth, but we anticipate that this optimal value won’t be identical to the noiseless case.

4.2 Noisy Simulations and Results

Having gained an understanding of the performance of wavefront coding in a noiseless system, we add noise to our simulation to mirror a likely physical scenario. We compare the results of the noisy simulation to the noiseless simulation discussed in the previous section. Any difference in the results from the two simulations is significant because it implies that the noise properties of a system alter the ideal system parameters and must be understood prior to the design process.

4.2.1 Temporal Noise Sources

Noise contributions in optical systems come from a variety of sources, each having an effect on the total noise level in the image. Temporal noise sources vary with time. We describe them using statistics instead of in absolute quantities because of their varying nature. Types of temporal noise include shot noise, reset and read noise, and dark current shot noise.

Shot noise is inherent in any signal and describes the variation in the number of photons arriving at the detector during a period of time. The probability of measuring a photon value, n, when $\bar{n}$ represents the average number of photons, is described using Poisson statistics as

$$p(n) = \frac{\bar{n}^n}{n!} e^{-\bar{n}}.$$

Equation 9

The average value of a Poisson distribution is also equal to the variance,

$$\Delta n^2 = \bar{n},$$

Equation 10

and the signal-to-noise ratio then becomes the square root of this mean value,

$$SNR = \sqrt{\bar{n}}.$$

Equation 11

For example, a 100 photon signal will have a shot noise level of 10 photons and a SNR of 10. For values of n >> 1, the Poisson distribution approximates a Gaussian distribution.

Read noise is a collective term encompassing the additive temporal noise sources associated with reading out the signal on the detector. The conversion of an analog signal into a digital number is not perfectly repeatable, so a variation in pixel value is added to an image each time the detector is read. The electronics of the CCD themselves also add extra electrons providing another source of fluctuation in each pixel measurement.[26] These variations in readout include thermal noise, also called Johnson noise, and 1/f or flicker noise. In our simulation, and later our experiment, we will characterize read noise as a single parameter and will not separate out the different sources.

Dark current noise is a measure of the number of electrons collected by a pixel as a result of thermal agitation at temperatures above absolute zero . This process causes non-zero pixel values to be measured even in the absence of any optical signal. The temporal noise associated with dark current has a Poisson distribution and is proportional to the square root of the dark current itself. Because dark current noise is strongly correlated with the temperature of the CCD, we can limit this contribution by cooling the detector. Our simulations required very short exposure times of less than a second, so dark current noise was a negligible factor; however, astronomical images requiring exposures on the order of many minutes are strongly affected by this source of noise. It is important to note, however, that prior to an exposure, dark current and background signal cause a collection of electrons in the detector. If the detector is left idle for a long period of time before an exposure is taken, a significant level of charge could build up creating a large noise contribution to the image. To prevent this, the detector must be background wiped; the CCD is read quickly and the charge on each pixel dumped before beginning the actual exposure.[26]

4.2.2 Spatial Noise Sources

Spatial noise sources cannot be reduced by averaging multiple images, as they remain constant over time. These sources are often collectively called fixed pattern noise and vary spatially across the detector, instead of temporally. Fixed pattern noise consists of individual hot (brighter) and cold (darker) pixels, which remain consistent across multiple exposures with the same illumination conditions. Causes of spatial noise include dark signal non-uniformity (DSNU) and photo response non-uniformity (PRNU). DSNU describes an individual pixel’s departure from the average in the absence of external illumination. The measured departure may change with a change in temperature or exposure time, however. PRNU arises from the fact that individual pixels of the detector do not all possess an equivalent sensitivity to light. Under uniform illumination, this pixel-by-pixel response variation causes output variation in the image.[27]

Spatial noise sources can be characterized and often minimized experimentally during the image flat fielding process. This process involves capturing a dark or bias reference and a uniformly illuminated flat reference and removing the contributions of both from the experimental image. The process we used is discussed with respect to the experimental procedure in Chapter 6.

4.2.3 Bias

Bias is not a random noise contribution, but we include it in this discussion because it adds a value to each pixel in the image sensor that is not directly caused by photons. An unexposed pixel will be represented, after readout and conversion into a digital value, by a value with a small distribution around zero. This distribution, caused by the readout and conversion noise, creates negative values in the image frame. Bias is a positive offset value assigned to each pixel before each exposure designed to eliminate the potential for negative values.[26] When the image is flat fielded, a pattern template is removed, thus removing bias from the corrected flat image.

4.2.4 Signal to Noise Ratio

The signal to noise ratio of an image taken with a CCD can be expressed in terms of the contributions from different noise sources and the desired signal as follows [26]:

$$SNR = \frac{N_*}{\sqrt{N_* + n_{pix}(N_S + N_D + N_R^2)}}$$

Equation 12

Here, N_* refers to the total number of photons in the desired signal, n_{pix} is the number of pixels included in the SNR measurement, N_S is the number of photons per pixel from the background, N_D is the number of electrons per pixel from the dark current and N_R is the number of electrons per pixel caused by the read noise. We assume in this equation that one photon incident on a pixel produces one electron. When we make SNR measurements later, we choose an area of flat illumination and use the average pixel and noise value across this region. In this case, npix is equal to one in the equation above.

4.2.5 Noise in the Matlab Model

Since we did not deal with photon counting applications or any extremely low light levels, we chose to use Gaussian statistics to simulate noise in our model. The probability of recording a value, n, assuming a Gaussian distribution is as follows,

$$P(n) = \frac{1}{\sigma\sqrt{2\pi}} e^{\frac{-(n-\bar{n})^2}{2\sigma^2}}.$$

Equation 13

Here, $\bar{n}$ again represents the average value of n, while σ^2 is the variance. As described earlier, using a Gaussian distribution to approximate shot noise is appropriate when $n >> 1$. Therefore, this approximation is appropriate for SNR values of about 10 and above ($n = 100$) but becomes less accurate as the SNR value decreases toward zero. Noise was added to our Matlab model using a zero mean Gaussian distribution with a specified normalized variance. We chose our specified noise variance based upon the desired image SNR,

$$\sigma_{noise}^2 = \frac{\sigma_{object}^2}{SNR}.$$

Equation 14

4.2.6 Optimal amount of cubic phase

Phase was added in the pupil of the optical system, depressing the MTF across the entire wavelength band, but simultaneously making the MTFs for each wavelength more uniform. As shown in the previous section, the MTFs became more uniform across a broader wavelength band as the amount of added phase increased, but also became more depressed. This MTF uniformity is what allows for performance improvements after applying the deconvolution algorithm. However, depressing the MTF curves too much caused the noise effects to be amplified, resulting in a worse overall performance. A comparison of noiseless and noisy broadband MTF curves is shown in Figure 15. The noise floor in this figure appears to remain at around 10% contrast, so signals that drop to this level and below are indistinguishable from noise. Thus, the phase surface design is a trade-off between increasing the wavelength band of the system while maintaining an MTF level high enough to remain above the noise floor. We ran a simulation to determine the ideal amount of phase that will provide the best recovered image.

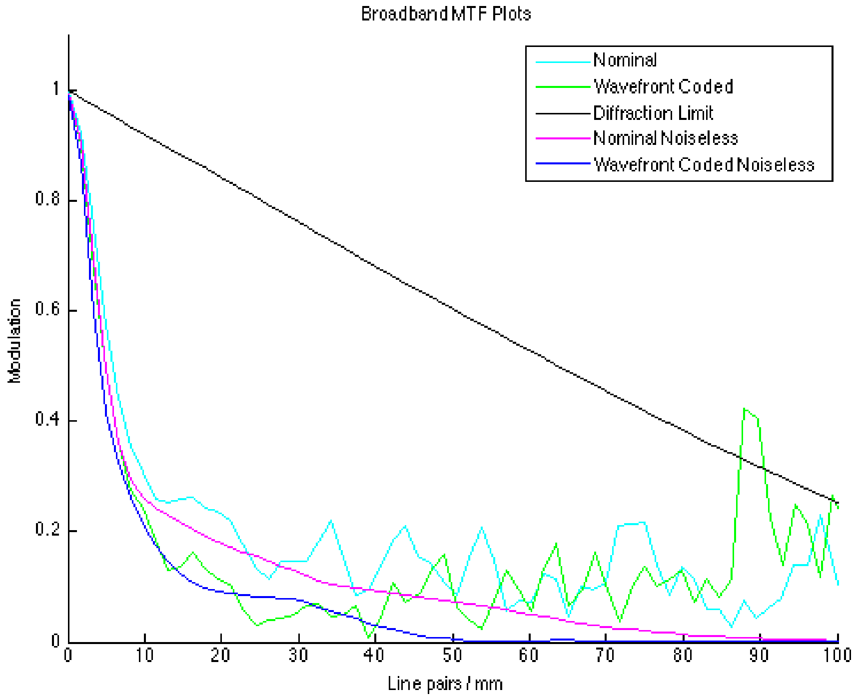

Figure 15: Shown is a comparison of broadband MTF curves with and without noise present.

4.2.6.1 Simulation Parameters

Images were simulated and reconstructed using the singlet lens and a cubic phase plate with varying phase amounts. The recovered image was evaluated using our previously discussed error metrics: RMSE and two versions of the MTFIA. Results of each error metric were then plotted to determine the optimal phase amount. This simulation was repeated for different SNR values to show how the optimal phase amount changes with noise in the nominal system. The simulation was also performed using a few different illumination bandwidths.

4.2.6.2 Optimal phase results

Figure 16 shows the results of our simulation using spectral broadband illumination and varying SNRs. The minimum RMSE value in Figure 16a designates the optimal amount of phase for each curve. We see that the blue curve, representing the system with the highest amount of noise, shows a clear optimal value of phase of 70µm sag. The pink and black curves, representing systems with lower noise levels, have a higher optimal phase value of 100µm. Figure 16b shows results for the same system, using the MTF integrated area metric, and arrives at the same optimal phase values. These results support our hypothesis that there is a trade-off between adding enough phase to correct the full wavelength range, while not adding too much phase that the MTF curves drop below the noise floor. This simulation also highlights the need to consider detected image noise during the optical system design process.

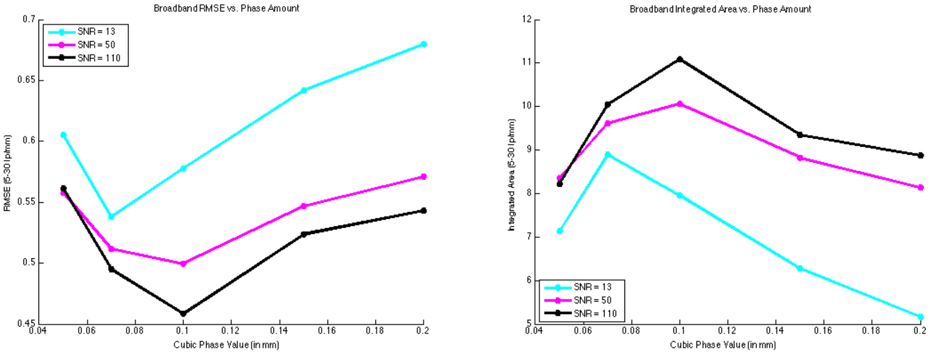

Figure 16: Wiener filtered images evaluated from an optical singlet with varying amounts of cubic phase added. Illumination was broadband, 3501100 nm. The three curves represent different SNR values. (a) RMSE evaluation; minimum value (b) MTFIA evaluation; maximum indicates best performing system. value indicates best performing system.

We then ran the same analysis using mid-bandwidth spectral illumination (400-570 nm). Results of this analysis are shown in Figure 17 and follow a pattern similar to the broadband illumination. For the mid-bandwidth system, both the RMSE error metric and MTFIA error metric point to an optimal phase value of 50μm for the highest noise case and 70μm for the medium and low noise cases. In both illumination cases, the optimal phase amount is smaller for the high noise system. Comparing results from Figures 16 and 17, we note that the optimal phase amount varies also with illumination bandwidth. As we saw in the previous chapter for noiseless systems, more phase is required to correct for a larger wavelength band.

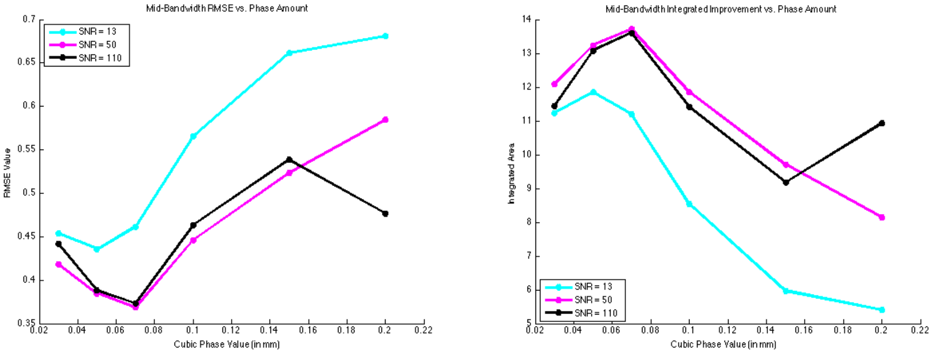

Figure 17: Wiener filtered images evaluated from an optical singlet with varying amounts of cubic phase added. Illumination was a medium sized bandwidth 400-570 nm. The three curves represent different SNR values. (a) RMSE evaluation; minimum value indicates best performing system.(b) MTFIA evaluation; maximum value indicates best performing system.

4.2.7 SNR Cutoff

Wavefront coding spreads out energy from the PSF across a larger area at the image plane making these systems more susceptible to noise. Because we attempt to boost the information content by first lowering contrast to make it more uniform, the deconvolution algorithms begin with a noisier signal than would be seen in a traditional optical system. Careful design of the deconvolution algorithm can minimize the increase of noise in the processed image, but cannot eliminate this problem completely.[28] Therefore, we ran a simulation to determine the minimum SNR that an image could contain before processing where the wavefront coding and deconvolution algorithm still resulted in a measurable benefit to the system.

A simulation of noisy wavefront coded images and corresponding reconstruction images was performed to determine this minimum signal to noise ratio required in a WFC system before image processing. In order to match our experimental results (presented in the following chapter), we used our achromatic doublet and the measured cubic phase modeled to our experimental phase plate. We introduced zero-mean Gaussian additive noise to the down-sampled simulated image (which has 5.5 µm pixels). In order to simulate different image noise levels, we changed the variance of the Gaussian noise and then measured the resulting signal-to-noise ratio. Because our images contained large areas of high pixel intensity, we were able to directly measure the SNR. We selected a rectangular region within one of these high intensity patches. For an accurate SNR measurement, the selected region must contain no modulation other than that caused by noise. We then divided the average intensity across these pixels by the standard deviation:

$$SNR = \frac{mean(selection)}{standard\ deviation(selection)}.$$

Equation 15

Our simulated images show the amplification of noise caused by the deconvolution filter applied to the captured image. For each reported SNR value, we simulated a nominal noisy image, then reconstructed it using our deconvolution algorithm. Finally, we extracted the MTF curves for spatial frequencies ranging from zero to the diffraction limited cutoff of the nominal system. Figure 18 shows the original image with an SNR of 12 and its corresponding reconstructed image. The starting SNR in this case is too low, and when noise is amplified by the deconvolution algorithm, there is a significant loss of contrast in the final image.

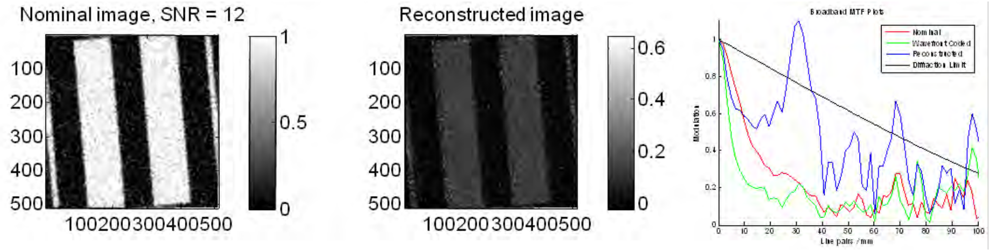

Figure 18: Simulation of a nominal image with a SNR of 12. MTF (right) shows noise is amplified and occludes signal.

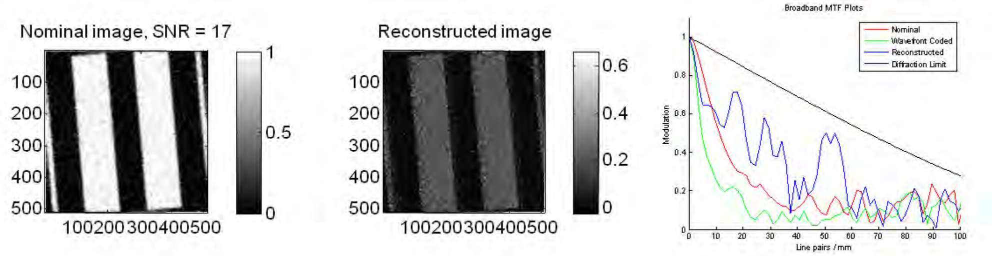

Figure 19: Simulation of a nominal image with a SNR of 17.

Figure 19 shows an image and reconstruction with a starting SNR of 17. In these images, it is apparent that, while noise amplification is still a dominant effect, there is also a notable contrast increase at lower spatial frequencies. An image with an SNR close to this value is at the lower boundary of where cubic phase is beneficial to a system.

Figure 20 shows an image with a high starting SNR of 28. Noise is still amplified in the reconstructed image by the deconvolution algorithm, but it is much less apparent than in the first two cases. The increase in noise here is an acceptable tradeoff for the boost in contrast given to a range of spatial frequencies.

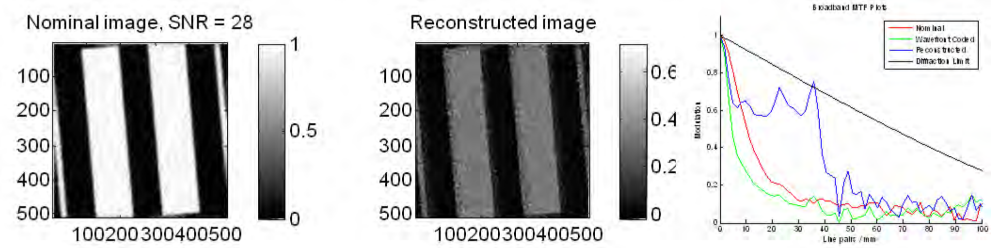

Figure 20: Simulation of a nominal image with a SNR of 28.

4.2.8 Conclusions on noisy systems

The addition of noise to our optical system model effected a change in the simulated optimal phase value regardless of illumination bandwidth. In a noiseless system, the designer must only take care to avoid zero or near-zero values in the deconvolution filter. However, in a noisy system, we conclude that the designer must also avoid letting the deconvolution filter fall below the noise floor or noise will be amplified in the final image. Noise, then, lowers the optimal phase value, and systems with more noise have a lower optimal phase than systems with less noise. This result implies that lens designers must understand the expected noise level of their nominal system image prior to designing the optical system. This conclusion runs contrary to the typical design process where noise is analyzed as a completely separate entity from the optics.

5. EXPERIMENTS

To validate our model, an experimental setup was designed to compare against our simulation. The simulation was also adjusted to mirror the actual experimental parameters. In this chapter, we will discuss the experimental procedure and analyze the results in comparison with the simulated experiment.

5.1. Experimental Test Bed

The final iteration of the experimental setup is shown in Figure 21. A singlet or doublet lens was mounted on a fixed stage, and the object was placed at a distance of 860 mm. The lenses both had approximately a 100 mm focal length and are used at an effective (working) F/# between 4 and 10. To set the F/#, we placed an adjustable aperture near the lens. The aperture diameter was varied between 20 mm for an F/4 system and 8 mm for an F/10 system. The doublet lens is used in the results presented here. The doublet was aligned using an alignment laser to less than 1/2" over a distance of four feet, corresponding to an alignment accuracy of 0.6 degrees.

We used an incoherent white light source with four heads to illuminate our diffuse object. The white light source had a color temperature of 3250K. The heads were spaced equally at an axial distance of approximately 32cm from the object and illuminated the object at 30 degrees with respect to surface normal. Figure 21a shows the positioning of the fiber bundle heads. The goal was uniform illumination across the camera's field of view at the object plane. A variety of different filters were placed in the illumination pathway so their optical properties did not impact the imaging properties of the system. Bandpass filters (Newport), with a full width, half-max (FWHM) of 10 nm, were used to simulate single wavelengths. Broadband illumination was achieved by using the unfiltered light source.

Alternately, a pinhole was placed in the same object plane to act as a point source, facilitating the acquisition of point spread function images. The pinhole was 25 μm in diameter and was back-illuminated by a focused fiber bundle. The pinhole and illumination setup was positioned on a motorized X-Y translation stage and was moved to various field positions in the object plane. The step motor driving the translation stage was measured accurately to 10 nm, but for the purposes of this experimental work, steps smaller than 0.1 mm were not necessary.

For capturing images, we used a cooled MicroLine ML1050 CCD camera from Finger Lakes Instrumentation (FLI), in Lima, New York. The camera included a Kodak KAI-01050 monochrome image sensor containing 5.5 μm square pixels and a micro-lens array placed in front of the detector allowing for a unity pixel fill factor. The camera had usable pixel values between the bias floor of about 2000 counts to the saturation level of 22,280 counts. The bias level was measured by examining the statistics of a bias frame, and the saturation level was tested and quoted on the camera's data sheet provided by FLI. The camera's dynamic range of just over 20,000 counts, then, allowed for capturing 14-bit images.

The camera position was controlled in three dimensions (X, Y, and Z) by a motorized stage. Using a stopped down aperture and our system alignment laser, we aligned the camera to approximately 3mm over a distance of 1.8m. This corresponded to a rotational alignment accuracy of 0.1 degrees in X and Y . The camera was then centered about the optical axis using the same alignment laser and positioning the laser spot on the camera's center pixel. Likewise, alignment of the translation stage along the Z-axis was verified by translating the camera and ensuring that the laser spot did not shift from the center pixel. We were able to determine the camera's center pixel exactly, so the camera was centered about the axis to within 5.5μm.

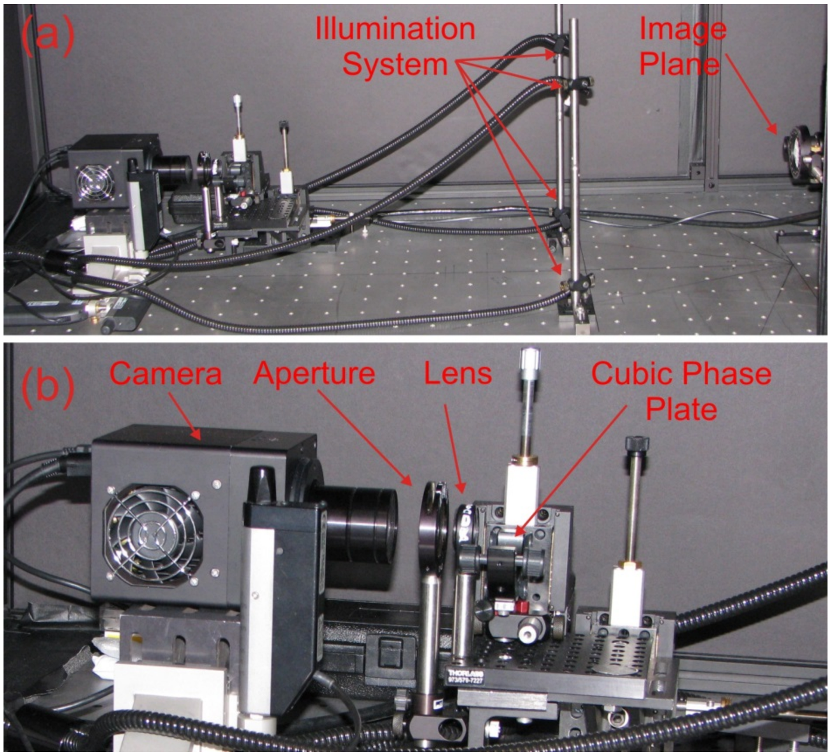

Figure 21: (a) wide view of experimental setup and (b) zoom in on camera, aperture, cubic phase plate, and lens.

The cubic phase plate was machined on a flat N-BK7 substrate by QED Technologies®, in Rochester, NY using the magnetorheological finishing process. The phase plate was placed approximately 8 mm on the object side of the lens. The aperture was placed on the image side of the lens at a distance of approximately 17 mm.

5.1.1. Aligning waveplate using PSFs

Proper placement of the waveplate into the optical train can be accomplished by imaging the PSF during the alignment procedure. Proper position needs to be aligned in both x and y (perpendicular to the optic axis), as well as properly rotated. The waveplate is properly aligned when the x and y streaks of the PSF, shown in some sample PSFs in Figure 22, stay aligned in x and y as well as remain equal in length when translating the waveplate through the full focal range (-1 mm to +1.4 mm).

A properly aligned PSF is shown in Figure 22. Note that the length of the legs is equal at each through focus position. An approximate alignment technique is as follows. While imaging the illuminated pinhole through the system with the aperture fully open, image the PSF in real-time on the camera. Insert the waveplate and rotate the waveplate so the x and y tails are aligned with x and y of the camera. This will give rotational alignment to about 1°. Now in an iterative fashion, move the focus and ensure that the length of the PSF “legs” stay equal through the whole focus. Small rotations and x-y displacements should be used to adjust the lengths. The overall size of the PSF can vary as long as it remains symmetrical on the diagonal. It is sometime helpful to slightly close the aperture to limit system aberrations. Converge on the proper position by noting whether the lengths get more or less equal with x-y displacement. Incorrect waveplate alignment will yield quickly varying and unequal PSF leg lengths as the focus is changed.

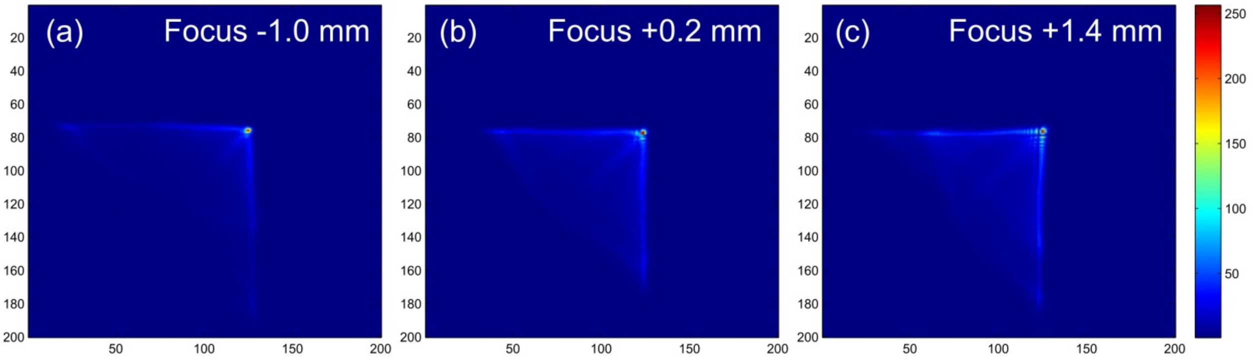

Figure 22: Through focus PSF of cubic phase plate at (a) -1.0 mm, (b) +0.2 mm, and (c) and +1.4 mm.

We were ultimately able to find a plate alignment position where the PSF remained symmetric through-focus. We later discuss a parametric optimization where we correlated the experimental results with our Zemax simulation. Here, after a great deal of analysis, we are able to determine that the phase plate was likely decentered in our experimental setup by about 0.3mm in X and aligned in Y better than 0.1mm. The difficulties we faced in the alignment process illustrate one of the challenges of designing and building wavefront coded systems.

5.1.2. Measurement procedure

For each image that was taken, we followed the same procedure so that we could compare images against each other. For a given aperture size, focus, camera temperature, and illumination wavelength a series of images were taken. With the target illuminated, the camera exposure is adjusted to get the maximum pixel count to close to 22,000 to avoid saturation and non-linear response of the camera. The image was taken at this exposure, followed by a bright field image (inserting pure white card stock at the image plane) and a dark field image (turning illumination off, but leaving exposure alone). The final image could then be calibrated properly using both the dark and bright field exposure.

5.2. Sample images

Samples of the images were taken at various focal distances, wavelengths, and temperatures to demonstrate the system. Figure 23 shows a sample image of both the conventional image compared to the wavefront encoded image.

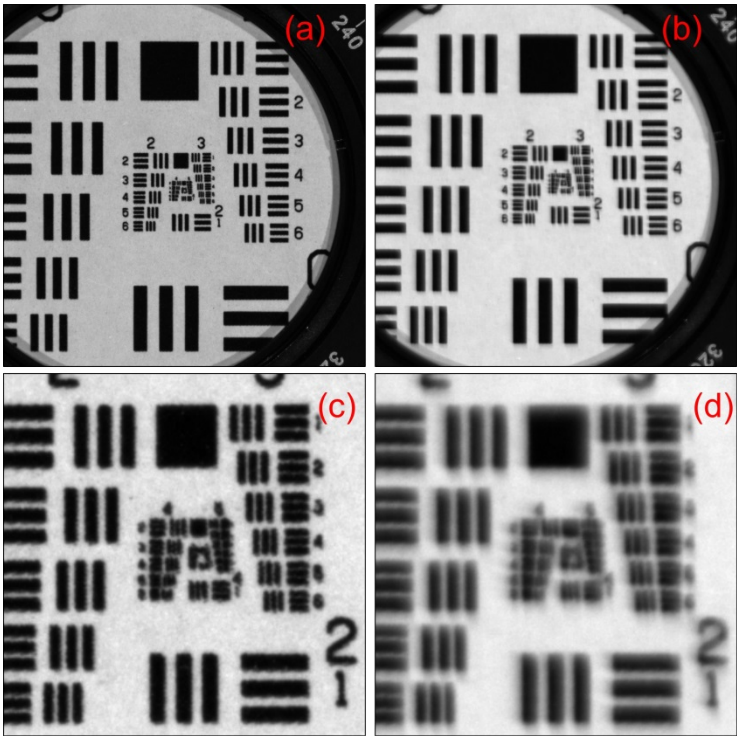

Figure 23. Two images at optimal focus illuminated by 500 nm light in large area (a,b) and zoomed (c,d). Conventional images are in (a) and (c) while wavefront coded images are in (b) and (d).

5.3. Metrology of fabricated waveplate

The cubic phase plate fabricated by QED Technologies (Rochester, NY) using magneto-rheological finishing was used to wavefront code the experiments. The manufacturers included white light interferometry (WLI) characterization of the waveplate shown in Figure 24(a) which was complemented by data taken with a coordinate measurement machine (CMM) here at Sandia shown in Figure 25.

The fabricated waveplate was manufactured according to the ideal surface

$$Z = 40\mu m\left(\left(\frac{x}{12.5}\right)^3 + \left(\frac{y}{12.5}\right)^3\right) - 24\mu m\left(\left(\frac{x}{12.5}\right) + \left(\frac{y}{12.5}\right)\right)$$

Equation 16

which is a cubic with a linear term removed where x and y are given in mm, the normalization factor of 12.5 is in mm, and the resulting Z is in microns.

Both the white light interferometry data and the CMM data fit to the ideal surface by minimizing the mean square error between the surfaces. The difference between the fabricated surface and the ideal surface for the WLI and the CMM in Figure 24(b) and Figure 25(b) respectively. Overlaid on this data is a circle of diameter 6, 8, and 10 mm. These rings are to illustrate that the discrepancies between the manufactured surface and the ideal surface is smallest in the middle portions of the waveplate, and increase as one moves toward the edges. This justifies the use of the 8 mm aperture in the experiments to exclude the wavefront errors introduced near the edges of the waveplate.

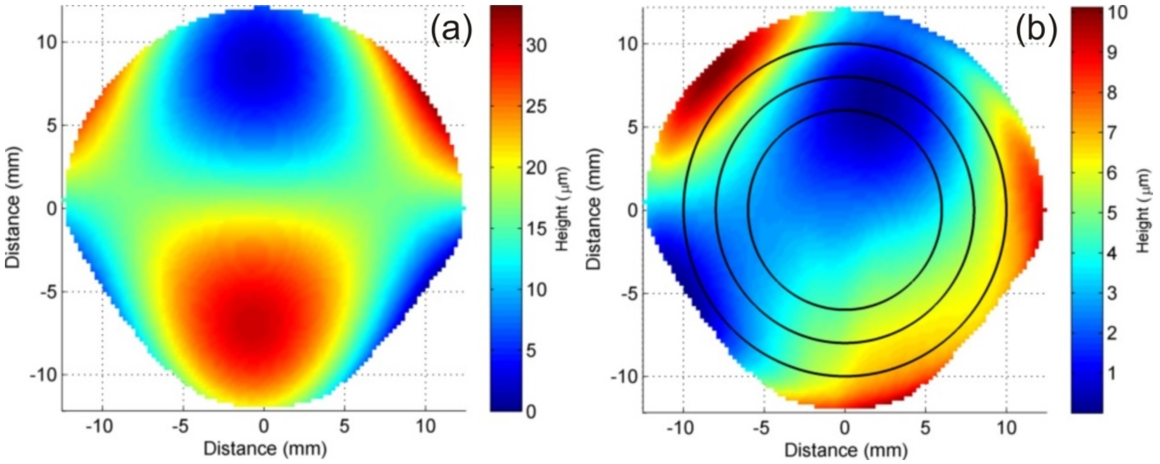

Figure 24. (a) white light interferometry measurements on fabricated waveplate and (b) difference between actual measurement and ideal surface form with diameters of 6, 8, and 10 mm overlaid.

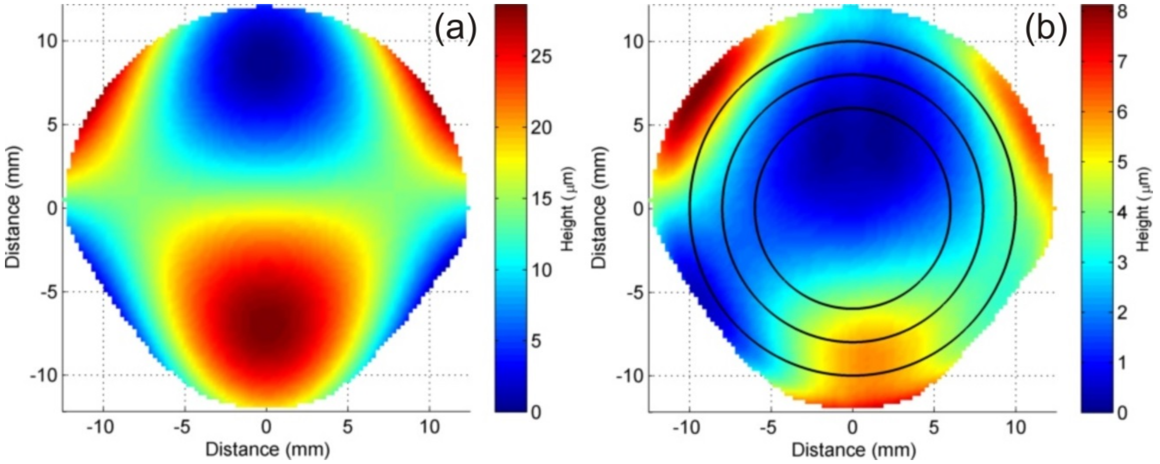

Figure 25. (a) coordinate measuring machine measurements on fabricated waveplate and (b) difference between actual measurement and ideal surface form with diameters of 6, 8, and 10 mm overlaid.

The measurements of the surfaces were fit to high order polynomials for import into Zemax for simulation of the PSFs. A plot of the difference between the polynomial fit and the CMM data is shown in Figure 26(a). The fit optimization tried to get less than a 50 nm difference between the polynomial fit and the surface at all points. Figure 26(b) shows how the fit criteria, the maximum height difference between measured surface and the polynomial fit, decreases with increased polynomial order. However, this improvement comes at a price of increased number of terms. For a 30th order fit, the polynomial has 496 terms for import.

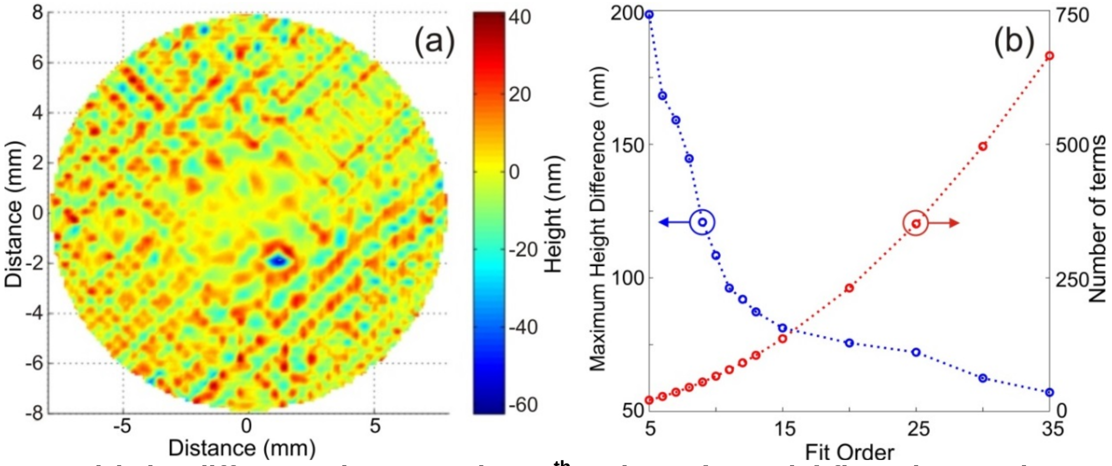

Figure 26. (a) the difference between the 30th order polynomial fit and CMM data and (b) the maximum height difference between the polynomial fit and the real surface compared to the number of terms as a function of fit order.

5.4. Noise of system

The temperature of the camera could be varied to introduce controllable amounts of noise into the images. This noise was quantified by imaging the standard resolution target as a function of both camera temperature which could vary from -30°C to 25°C and exposure time which varied from 1 ms to 300 ms. This signal to noise (SNR) level is shown as a function of exposure time at the extreme camera temperatures in Figure 27.

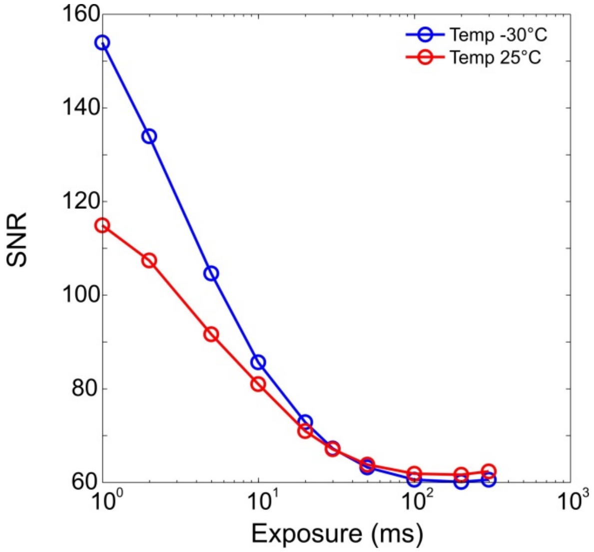

Figure 27. Signal to noise versus exposure time at the extreme camera temperatures

To determine the noise in the Zemax simulation, the total optical path including aperture, lens, and the resolution target at the imaging plane was simulated in Zemax geometric image analysis. A sample-generated image is shown in Figure 28(a) and the signal to noise of the image as a function of number of rays is shown in (b). Correlating the data in Figure 27 to that in Figure 28(b) can be used to determine parameters for imaging simulation.

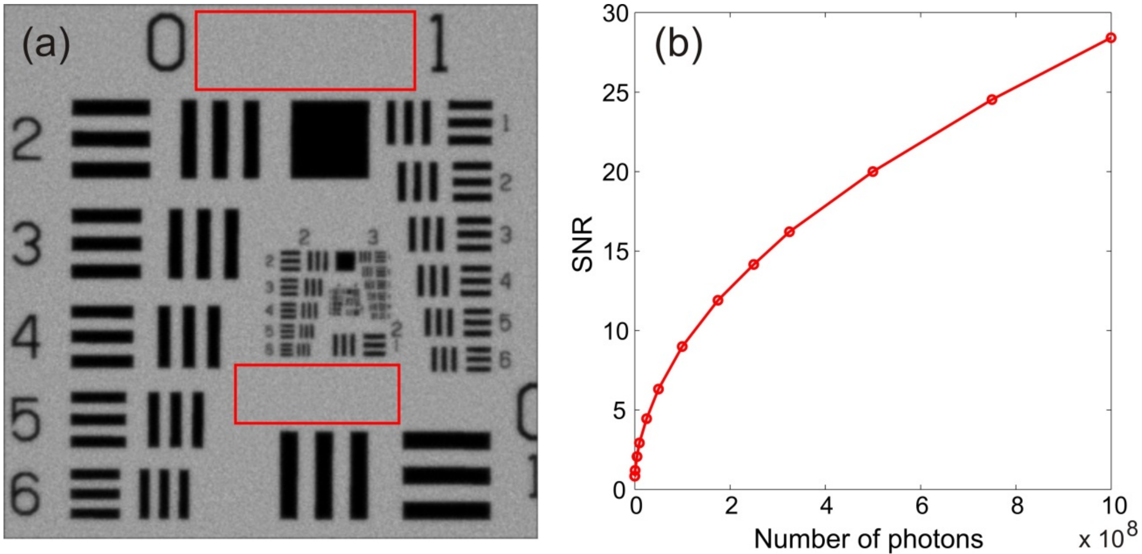

Figure 28. (a) Resolution target simulated by Zemax when illuminated by 10^5 photons and (b) the SNR of the red boxed region in (a) as a function of photons

5.5 Parametric Optimization

Parametric optimization refers to the process of correlating the alignment of the experimental system with the model in order to reliably compare the results. A parametric optimization was performed to match the alignment of the phase plate in the experimental setup with the Zemax model. An experimental system was set up using the 25 µm pinhole to serve as the object. A similar setup is used by Somayaji et al. [29] to measure cubic PSF images.

The diffraction-limited resolution of a system is described as

$$Res = \frac{1.22\lambda}{2NA},$$

Equation 17

which evaluates to approximately 6 µm assuming 500 nm illumination and a numerical aperture of 0.05. Further assuming the system is diffraction-limited, this resolution increases to approximately 2 µm when the aperture is opened to f/4. When the camera is placed in the focal plane of the pinhole, the system can resolve this pinhole and it cannot be considered a true point source. However, we simulated this setup in Zemax using a circular aperture as our object. We also note that our system is not diffraction limited once we leave the focal plane or introduce the phase plate to the system. In these cases, the approximation of our pinhole as a point source is valid.

5.5.1 Nominal System

We started with the nominal system to compare results of the simulation and experiment as well as to determine the position of best focus without the phase plate present. Axial alignment of the camera was matched by comparing a series of through-focus pinhole images at a few field points. Experimental images were taken at 200 μm focus steps, so the correlation between experiment and simulation will not be any more accurate than this step size. Figure 29 shows a through-focus series of on-axis pinhole images using 500 nm illumination. Figure 30 shows a similar series with the pinhole now located at the field position (13.9 mm, 13.9 mm). In both figures, simulated images were generated as geometrical images in Zemax using the circular aperture as the object. Both image series show a strong correlation between simulation and experiment. Using these two image series, we were able to establish that the axial position of best focus for 500nm illumination is located at 200 μm in the experimental setup.

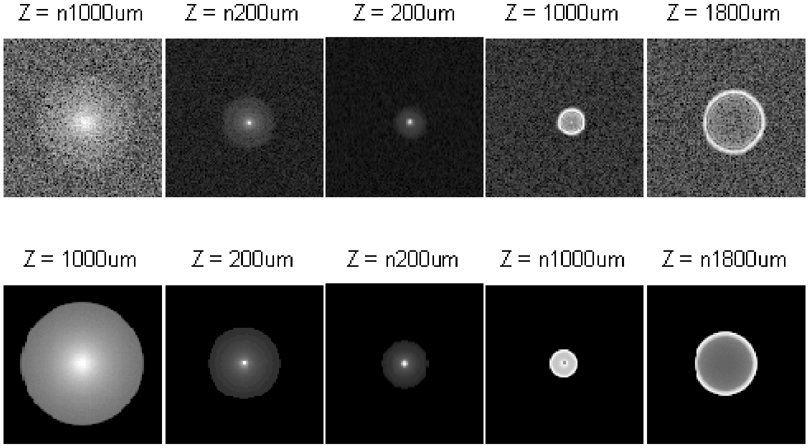

Figure 29. Comparing through-focus on-axis pinhole images shows good agreement between the simulation (bottom row) and the experiment (top row) for the doublet system with no phase plate. (Axial position is labeled for each image with respect to the zero position of the camera motor. A value of Z = n200um refers to a value of −200μm). Because of the sign convention in Zemax relative to the motor controller, there is a factor of −1 between the two values.

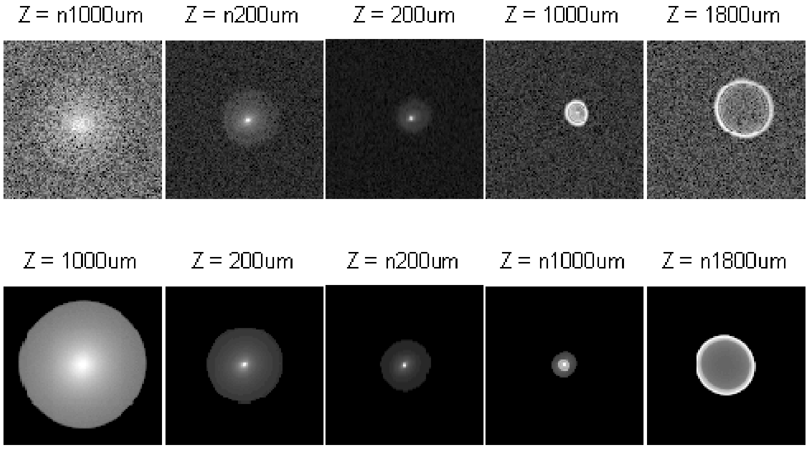

Figure 30. Through-focus pinhole images are compared for an image field point of X = 13.9 mm, Y = 13.9 mm. Experimental images (top row) agree well with simulated images (bottom row).

5.5.2 Wavefront coded system

Next, we compared our wavefront coded experimental images with the simulated images. The goal here was to determine the positioning and decenter of the phase plate. A similar process as the one described for the nominal system was used to correlate the alignment of the cubic phase plate in X and Y . However, since the alignment of the phase plate was unknown within a plane, instead of along a single axis, the parametric optimization process was more complicated. Pinhole image sequences were simulated for a decentration of the phase plate at each point within a 3X3 grid, centered about the optical axis and including steps of 0.3mm. This step size was used because it provided a visually apparent change in the pinhole image to allow for comparison, whereas a smaller step size was harder to distinguish. For each point on the grid, a through-focus image sequence was recorded for both an on-axis pinhole, as well as a full-field pinhole. These simulated image sequences were compared with the on-axis and full-field experimental image sequences. Using a few iterations of this process, simulating and then comparing image sequences, we were able to approximate the alignment of the experimental phase plate. Validation of this alignment is shown by the pinhole images in Figure 31. On-axis pinhole images are shown in Figure 31a, while Figure 31b shows images for a pinhole located at field position (X = 13.9mm,Y =13.9mm).

The alignment was visually best for the comparison shown in the picture, where the phase plate was decentered in both X and Y by 0.3 mm.

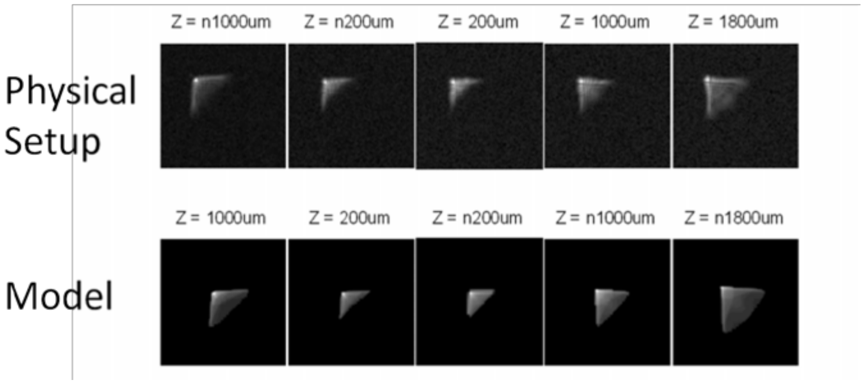

(a) On-axis pinhole images.

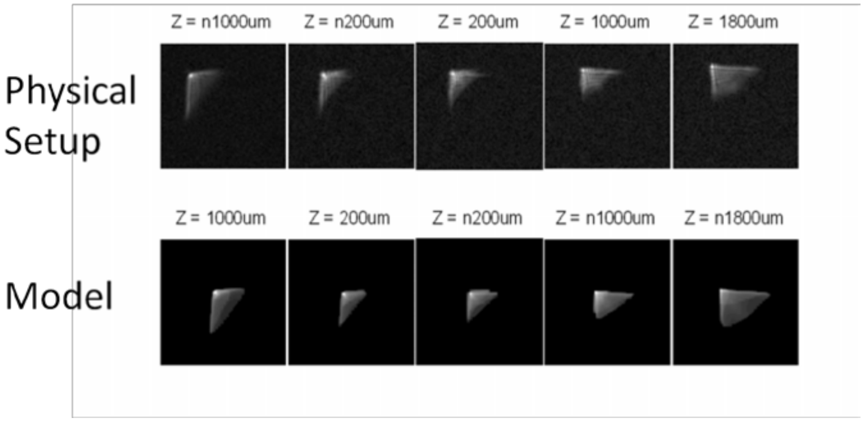

(b) Full-field pinhole images

Figure 31. After the parametric optimization and adjustment of the Zemax model to match the experiment, a comparison of simulated and experimental pinhole images, displayed as the cube root to highlight details, shows agreement in both overall geometrical shape and also small geometrical details.

5.6 Wavefront Coding and Aperture

Aperture size is an important first-order optical system parameter that drives the layout of an optical system. Understanding the impact of numerical aperture (or inversely, F/#) on the effectiveness of cubic phase is critical to the development of a wavefront coded system.

In the experimental setup, we captured images using two different F/#s, varied by changing the size of the aperture. At f/10, only an 11mm clear aperture of the phase plate is used, and therefore, the sag of the plate within the used aperture is relatively small. The map in Figure 32 shows the sag of the phase surface with this smaller clear aperture.

At larger apertures, the illuminated portion of the phase plate is larger, and the sag is much higher. As we used a cubic function, the sag increases by the cube of the increase in radius size. With a larger sag, the phase plate is harder to manufacture and becomes more prone to errors (departure from the designed surface) toward the edge of the part. In terms of manufacturability, the value of the sag does not necessarily determine the difficulty level of the part; instead, it is the maximum slope of the surface that causes a part to be easier or harder to manufacture. Since the phase plate is designed to be placed in the pupil, this sag to clear aperture ratio is directly determined by the numerical aperture.

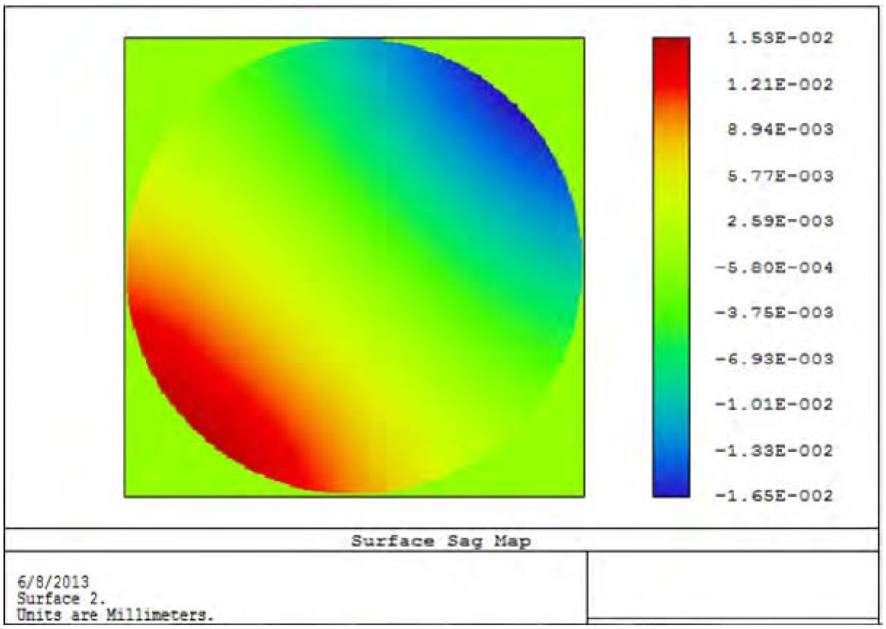

Figure 32. Zemax modeled sag of the phase plate surface with a clear aperture of approximately 11mm, which corresponds to an f/10 system.

Examining our experimental images, we noticed larger mismatches with simulated images as the aperture was increased. We found the fit required a 12th-order polynomial (91 terms) to bring the mismatch between the fit and actual surface below a quarter wave. From this fit, we determined that our phase plate contained significant departures from the designed surface toward the edge of the part. We began to see these large edge errors at around a 20mm clear aperture, highlighted in Figure 33. For this reason, we chose to limit our experimental image analysis to those images taken at F/10.

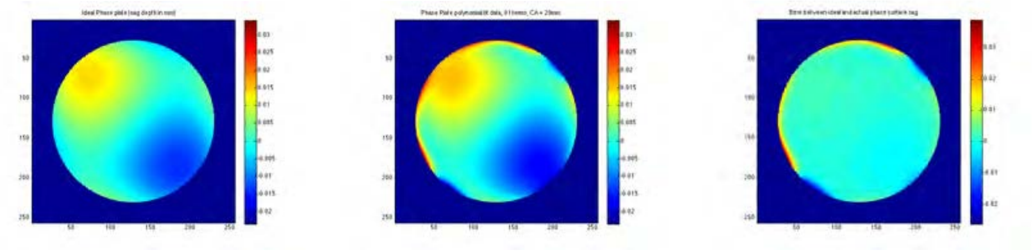

(a) Designed phase surface

(b) 12th order polynomial fit (91 terms)

(c) Error between fit and ideal surface

Figure 33. Ideal phase surface (a), physical surface polynomial fit (b) and error between the as-built and ideal surfaces (c) show large departures (peak-to-valley errors of over 50 µm) near the edge of the part for a 20 mm clear aperture.

For the experimental analysis, subsequently discussed, we used the achromatic doublet. We chose to capture all our experimental images herein using an F/10 system to minimize the impact of any physical departure from the ideal surface. Full-field images were obtained by replacing the pinhole with a diffuse object illuminated by a white light source and a fiber bundle split into four heads, as described previously.

6. RECONSTRUCTIONS OF EXPERIMENTAL DATA

Reconstruction of experimental images followed a slightly different procedure than with the simulated images. Experimental images required flat-fielding in order to reduce noise and remove illumination non-uniformity. Furthermore, pixel and array sizes between the recorded image and deconvolution PSF were matched. Reconstruction required using a simulated (from Zemax) rather than measured point spread function because of the camera's pixel size. The 5.5 µm pixels of the camera are too large to capture the PSF required for deconvolution. This sample spacing does not adequately resolve the patterned features of the PSF enough to recover the object, as discussed earlier in Chapter 3.

A higher resolution PSF could be measured using additional optics to magnify the original PSF on the camera, but this setup would add complexity to the experiment in a few ways. First of all, the magnification would need to be measured to a high degree of accuracy to be used in the reconstruction algorithm. Secondly, the additional optics would introduce a new set of aberrations, degrading the desired PSF and adding another level of uncertainty. This process, however, would have the advantage of removing the alignment uncertainty between the actual system PSF and the Zemax simulated PSF.

Instead, the solution we chose was to use the simulated PSF from Zemax for the as-built system and phase plate. The challenges in using the simulated Zemax PSF resided in alignment of the phase plate and modeling the experimental system very accurately. Figure 34 shows the algorithm layout, modified for experimental images.

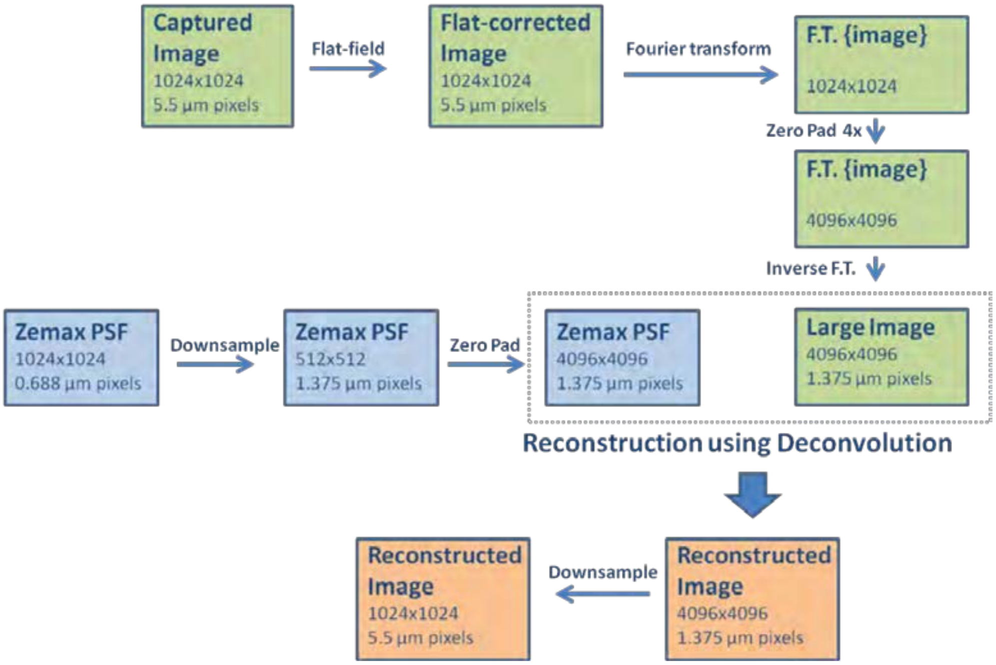

Figure 34. The experimental reconstruction algorithm begins with a captured image (green, upper left) and a simulated PSF (blue, middle left), adjusts each for matching array and pixel sizes, then uses deconvolution to produce the final reconstructed image (orange, bottom left).

6.1. Sample Reconstruction

The experimental data was reconstructed using the Matlab mathematical programming language. This relies on Matlab's internal fast Fourier transform (FFT) functions. Briefly, the experimental PSF is Fourier transformed to the optical transfer function (OTF) and appropriately filtered. This OTF is then convolved with the Fourier transformed wavefront coded image and the result is transformed back using the inverse Fourier transform into real space to yield the reconstructed image. An example of a complete series including the conventional, wavefront coded and reconstructed image is shown in Figure 35. A complete version of the reconstruction routine is given in Appendix A.

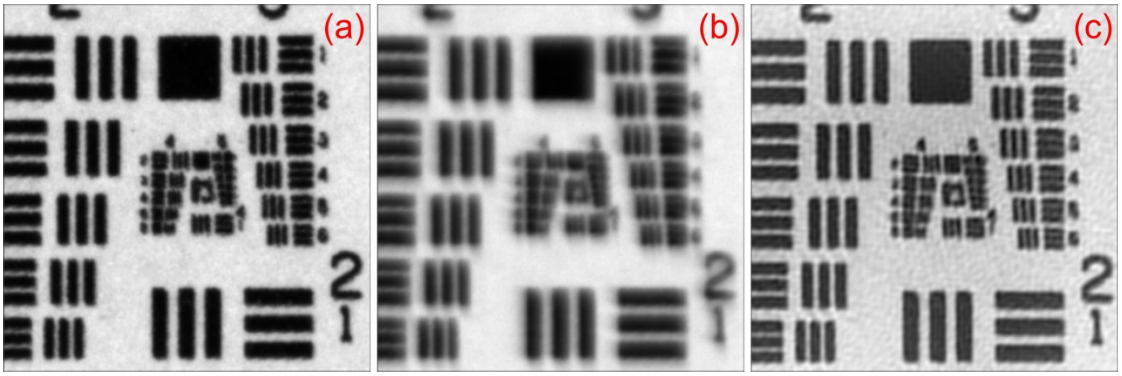

Figure 35. A series of images at 500 nm at optimal focus zoomed in on the smallest resolution bars for (a) the conventional image, (b) the wavefront coded image, and (c) the reconstructed wavefront coded image.

To evaluate the quality of the reconstructed image, the modulation transfer function (MTF) was calculated from the line pairs in the resolution target using the standard technique where the minimum and maximum contrast values for each line pair is calculated from

$$C(f) = \frac{C_{max} - C_{min}}{C_{max} + C_{min}} \qquad \text{Equation 1}$$

where C_{max} and C_{min} are the minimum and maximum contrast across a given line pair. The MTF is calculated by normalizing the individual contrasts by

$$MTF(f) = C(f)/C(0) \qquad \text{Equation 2}$$

where C(0) is the contrast of low frequency areas of the image (large uniform areas of contrast). An example of the automatic extraction routine implemented in individual line pairs implemented in Matlab is shown in Figure 36.

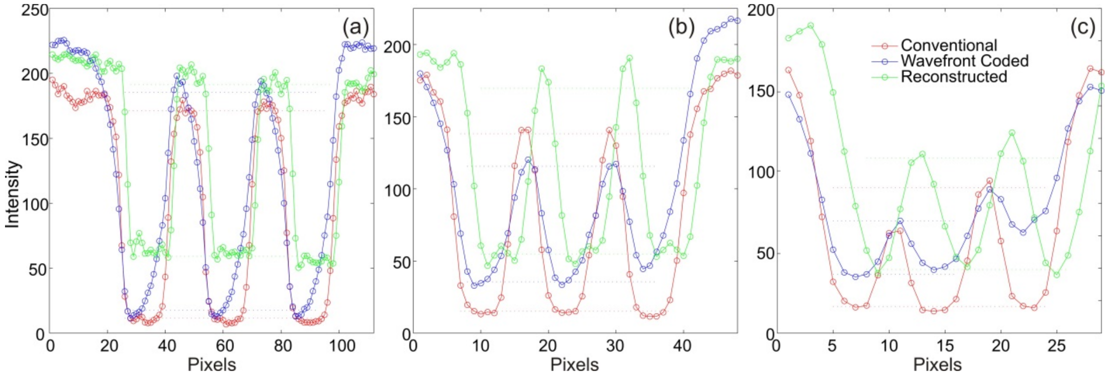

Figure 36. Contrast line scans for images in Figure 35 for line pairs of (a) 0.63 lines/mm (b) 1.41 lines/mm, and (c) 2.24 lines/mm

The MTF curves of the sample conventional, wavefront coded, and reconstructed images in Figure 35 are shown in Figure 36.

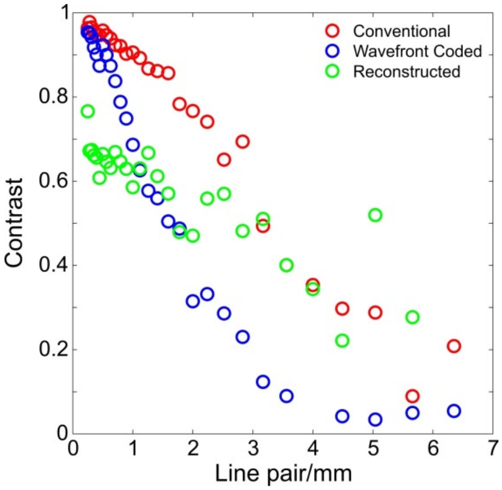

Figure 37. The MTF curves for the conventional, wavefront coded, and reconstructed images in Figure 35.

6.2 Experimental SNR Cutoff

Next, we captured a series of noisy experimental images to determine the impact of noise on the reconstructed image and to make sure our experimental results were consistent with the modeled analysis. In order to change the noise level, we varied the exposure length. For each image, the SNR was then determined by selecting an area of high intensity and performing the following calculation: [30]

$$SNR = \frac{mean(selection)}{standard\ deviation(selection)}.$$

Equation 18

Because we flat-field each image, we can be confident that the statistics of our high intensity selection are representative of the entire image. The first image, shown in Figure 38, was taken with a 1 ms exposure, corresponding to a nominal image SNR of 9. The image was reconstructed using a Wiener filter with a constant matched to the SNR to minimize noise amplification. In this image and subsequent images, our high intensity area is a rectangular selection from the lower right-hand corner of the image. Looking carefully at this figure, we see that the wavefront coded nominal image, shown on the left, contains information up to about 35 lp/mm, according to the blue curve in the MTF plot on the right. Noise in the nominal image destroys information above this spatial frequency. Noise amplification in the reconstruction causes almost all of this original information content to be lost, evidenced by looking at the green MTF curve. The contrast falls close to zero at a spatial frequency less than 10 lp/mm, and contrast above this frequency is likely caused only by noise. Furthermore, the SFR algorithm relies on being able to computationally locate the edge in the region of interest; in this case, the edge is obscured so much by noise, the algorithm fails. Visually, one can make out a minimal level of contrast for the lowest spatial frequencies; however, the nominal image is clearly more visually desirable. Consequently, an image with an initial SNR that is too low, evidenced by this example, will not benefit from wavefront coding; information will be obscured by the noise. The maximum intensity pixel of the experimental images was normalized to one prior to reconstruction. The reconstructed images were not re-scaled; when noise was amplified, the resulting images appeared darker.

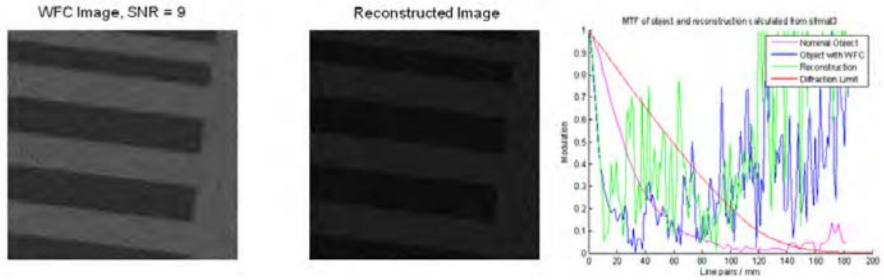

Figure 38. Experimental wavefront coded image before processing (left) and reconstruction (middle) taken with a 1 ms exposure, corresponding to a SNR of 9. MTF (right) shows noise is amplified and occludes signal.

The next set of images in Figure 39 represents a 3 ms exposure. The signal to noise ratio in the wavefront coded image has increased to 13 by extending the exposure time. Looking at the reconstruction, it is evident that noise is still amplified in the final image. However, some of the spatial frequencies are boosted causing a greater overall information content within a limited spatial frequency range. This exposure, and corresponding SNR, represents a case very close to the cutoff of where wavefront coding provides a benefit. Depending on the application, the increase in noise in the final image may or may not be tolerable.

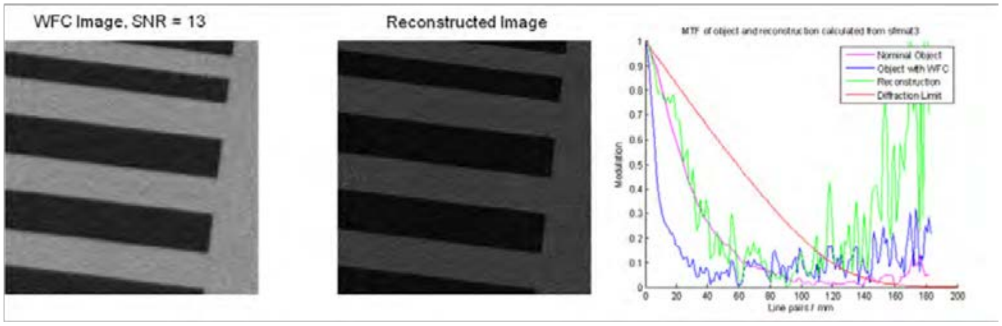

Figure 39. Experimental wavefront coded image before processing (left) and reconstruction (middle) taken with a 3 ms exposure and a SNR of 13. This image is just at the SNR cutoff for a wavefront coded system. MTF (right) shows increased contrast in lower spatial frequencies, but also significantly increased noise in higher frequencies.

The final set of images, shown in Figure 40, were taken with a much higher exposure (20 ms). The SNR is increased to 30. This case represents a system which may benefit significantly from wavefront coding, as noise amplification is not a limiting factor. The MTF curves for this case demonstrate that the information content of the reconstruction receives a boost up to about 70 lp/mm with almost no noise amplification below this spatial frequency cutoff. Higher spatial frequencies receive only a small amount of noise amplification.

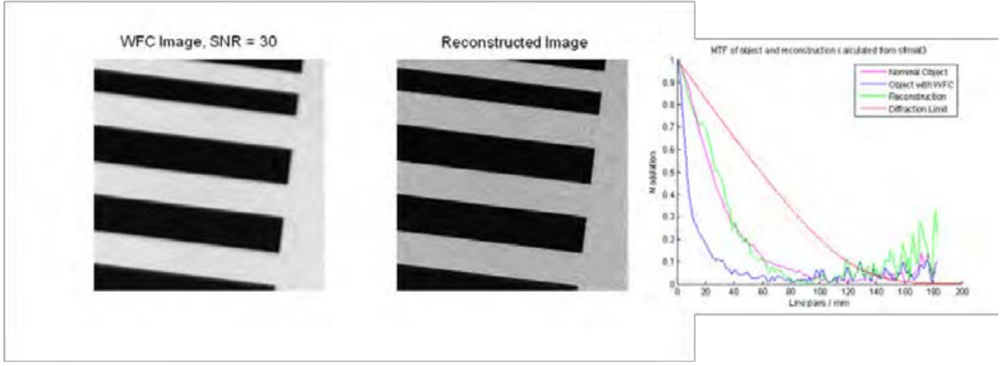

Figure 40. Experimental wavefront coded image before processing (left) and reconstruction (middle) taken with a 20 ms exposure and a SNR of 30. Spatial frequencies in MTF plot (right) are boosted, while noise is only minimally increased.

To demonstrate that our imaging algorithm does not depend on the object, we image and reconstruct two other objects: a resolution target and a portion of a grey-scale scene. These images were each recorded with a broadband exposure time of 20 msec. The SNR of the highest intensity portions of these images was 30, the same as our grid targets. Figure 41 displays the wavefront coded (left) and reconstructed (right) images of the resolution bar target based upon the US Air Force 1951 standard. Blocks of three bars are displayed both horizontally and vertically at varying spatial frequencies. The resolution target is generally used to determine the spatial frequency cutoff; the largest block of bars that is unresolvable in the image determines this value. In Figure 41, we zoom in on the high frequency portion of the resolution target. Likewise, Figure 42 shows a portion of a scene with wavefront coding (left) and the reconstructed image (right).

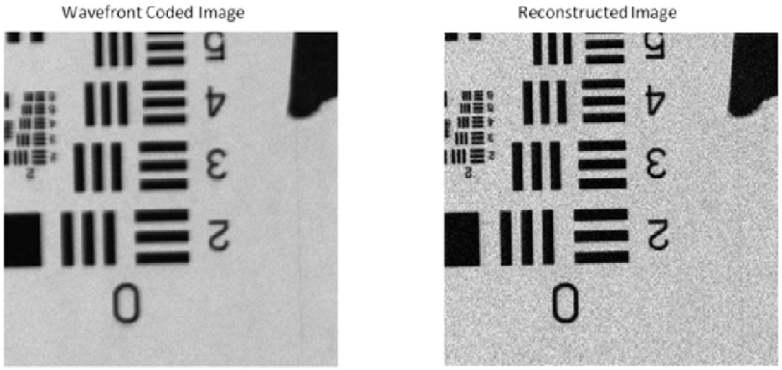

Figure 41. The object for these two images is a resolution bar target based upon the USAF-1951 standard. Nominal image on the left is a 20 msec exposure from the wavefront coded system before reconstruction. The SNR is 30, the same as our previous 20msec exposure of the grid target. The reconstructed image on the right appears crisper, but does have an increased noise level.

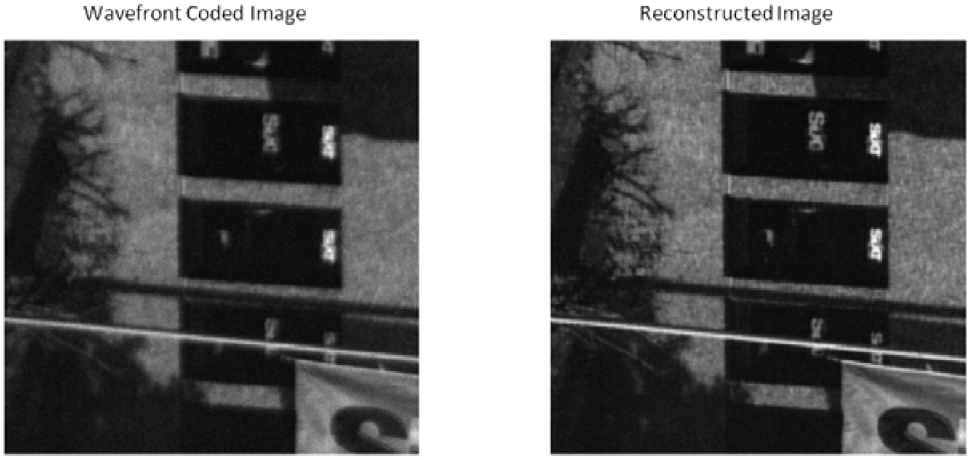

Figure 42. A section of a grey-scale scene is used as the object for these figures. Looking particularly at the white letters toward the right-hand side of each image, the resolution is enhanced in the reconstructed image.

6.3. Optimization of Reconstruction Parameters

The automatic extraction of the MTF data from the reconstructed images allows for rapid optimization of the extraction parameters. The reconstruction parameters included threshold and gamma used in the filtering of the OTF of the experimentally acquired PSF and a smoothing kernel size used in the inverse filter. Standard settings, which were close to optimized, for the parameters where a threshold of 0.001, a gamma of 1, and a smoothing kernel of 11.

Each parameter was investigated independently to determine the effect on the reconstruction quality. The quality of the reconstruction was determined by calculating the change in contrast for selected line pairs, the SNR of the image, and the area under the MTF curve. Looking simultaneously at three different metrics gave a better indication on the quality of the reconstruction. Discussion of both the threshold and smoothing kernel is discussed below. It was found that gamma had negligible influence on the reconstruction.

The optimization of the threshold parameter is shown in Figure 43. As the threshold value is varied around the nominal value (0.001) the influence on the line contrast of the individual pairs (Figure 43(a)), the SNR of the image (Figure 43(b), and the area under the MTF curve (Figure 43(c)) can be examined.

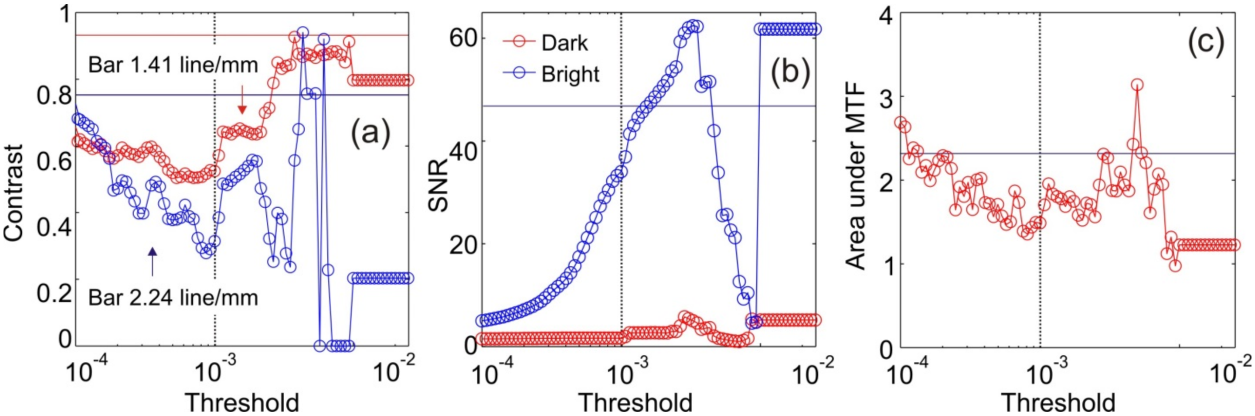

Figure 43. Variation of the (a) contrast of individual line pairs, (b) SNR, and (c) area under the MTF curves as a function of varying threshold. Horizontal bars indicate the conventional image value(s), and vertical line indicates the nominal setting of threshold.

Sample reconstructions are shown using different threshold values in Figure 44. The reconstruction in Figure 44(a) show a threshold value on the left edge in Figure 43 while that in (c) is from the right edge where the reconstruction becomes insensitive to threshold. Figure 44(b) shows a reconstruction from near the peak of the SNR in Figure 43(b). It is clear that while the SNR improves significantly above the conventional image, the contrast of the reconstructed image does not.

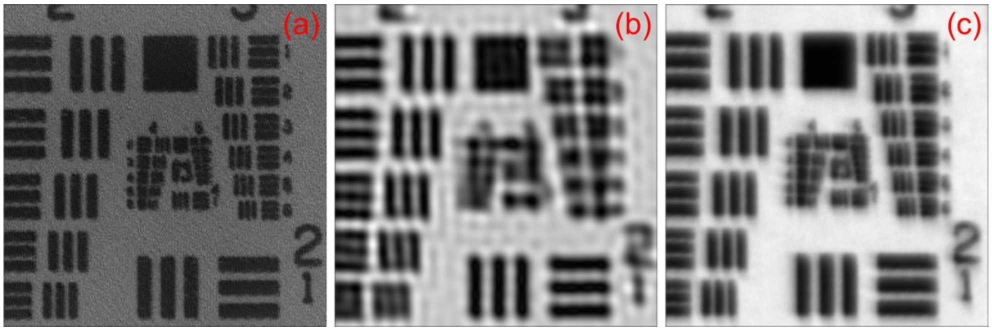

Figure 44. Sample reconstructions for thresholds at (a) 1x10^{-5}, (b) 0.003, and (c) 0.02 with other parameters at default values.

A similar optimization of the smoothing kernel is shown in Figure 45. Sample reconstructions near the low and high values of smoothing kernel are shown in Figure 46.

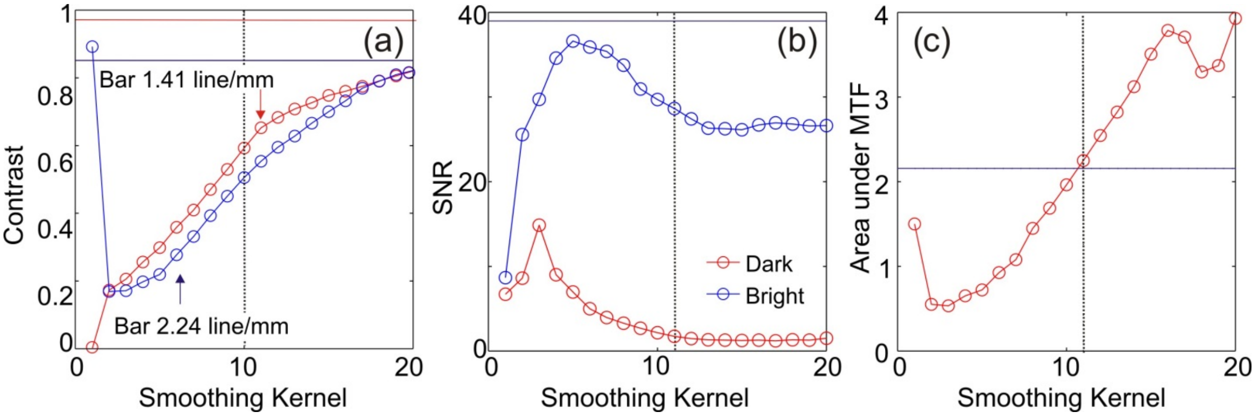

Figure 45. Variation of the (a) contrast of individual line pairs, (b) SNR, and (c) area under the MTF curves as a function of varying threshold. Horizontal bars indicate the respective value(s) taken from the conventional image values, and vertical line indicates the nominal setting of smoothing kernel.

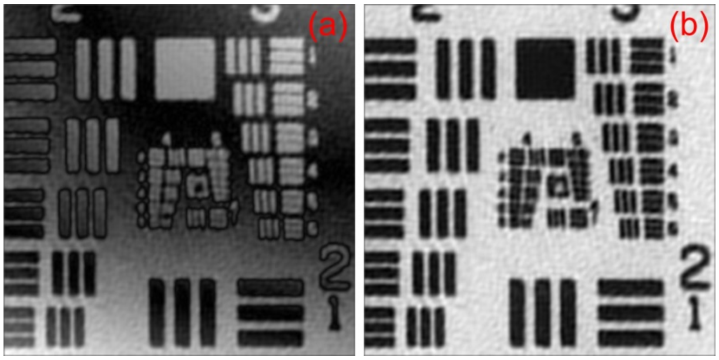

Figure 46. Sample reconstructions for smoothing kernel of (a) 1 and (b) 20 with other parameters at default values.

6.4 Conclusions

In both the noisy simulation and the experimental results, we were able to determine an approximate cutoff signal-to-noise ratio where wavefront coding began to show a benefit to an optical system. In the simulation, we determined this cutoff to be at an SNR of about 17, while in the experimental analysis, we found this SNR to be at around 13. The margin of error of this cutoff determination is around 20 % for a few reasons. We analyzed discrete exposure times and SNR values, so we only have data for these few values and must infer the system behavior in between. The cutoff is not a distinct boundary; instead, it provides more of a rule-of-thumb to guide lens designers. Finally, there exist many ways to evaluate images, of which we chose two to present. The image evaluation metric along with the statistical nature of noise cause any given perturbation of metric and system to arrive at a slight variation of cutoff SNR value. Within this margin of error, the results of the simulation and experiment provide a strong match.

7. DESIGN CONSIDERATIONS FOR CUBIC PHASE SYSTEMS

The optical system design process traditionally begins with a set of first-order constraints that help determine the system layout. These first-order parameters include bandwidth, aperture and field-of-view. In this thesis, we attempted to determine the ways in which these first-order parameters impact the performance of a wavefront coded system with cubic phase and how the parameters drive the design of such a system. We also showed that while not a traditional first-order parameter, noise drives the design of a cubic phase encoded system and must be considered along with the other preliminary constraints.

The results of this examination of wavefront coding performance in noisy broadband optical systems can be summarized into a set of design guidelines. Cubic phase is not ideal for all optical systems. Optical designers may want to keep these guidelines in mind when considering whether the addition of cubic phase and a reconstruction algorithm will be an effective method for increasing performance in their particular system.

7.1 Bandwidth

When considering wavefront coding to correct for axial chromatic aberration in a broadband system, the size of the illumination bandwidth directly influences the design of the cubic phase plate. We simulated optical systems with varying bandwidths to determine the ideal amount of phase in a noiseless and then a noisy system. The bandwidths evaluated included two medium-range bandwidths, 400−570nm and 500−660nm, and one wide bandwidth, 350−1100nm. We found that the larger bandwidth required a larger amount of phase for optimal reconstruction, while the best phase amount for the medium-range bandwidths was smaller. Furthermore, this result held true regardless of the noise level of the system. The amount of cubic phase determines the axial region of focus that can be corrected during reconstruction, assuming spherical aberration is negligible.

7.2 Aperture

Because the cubic phase in a wavefront coding system is placed in the pupil, the aperture size directly impacts the physical sag required to manufacture the phase plate. Assuming a circular clear-aperture requirement placed on the phase plate, the maximum sag value at the edge of the part scales as the cube of the aperture size.

Additionally, an increased numerical aperture limits the depth of focus of the nominal system. The wavefront error (optical path difference) at the edge of the pupil due to defocus is described by

$$\Delta W_{defocus} = \pm \frac{\epsilon_z}{8(F/\#)^2},$$

Equation 19

where ε_z is the depth of focus.[31] We showed that adding more cubic phase, in the form of a larger physical sag, brings a longer axial region into the reconstructed depth of focus of the system. Equation 19 implies that when the aperture size is increased, the depth of focus inherent to the system decreases, and additional phase is required for reconstruction, assuming all other system parameters remain the same. Using our experimental parameters, then, we calculate that the depth of focus of the F/10 aperture is 6.25X larger than the depth of focus for the same system at F/4.

In summary, increasing the aperture size affects the cubic phase plate in two ways. The sag of the part at the edge of its clear aperture increases as the cube of the aperture radius increase. Additionally, the designed amount of phase must be increased to compensate for a smaller nominal depth of focus. These two factors limit the effectiveness of wavefront coding with a cubic phase in a high NA system, such as a microscope objective. Experimentally, we successfully implemented reconstruction using a cubic phase in an F/10 system. We were unable, however, to demonstrate successful reconstruction of the same system at F/4 due to large departures in the phase surface from the designed surface.

Larger aperture systems, then, place additional constraints upon the design of the system for successful implementation of wavefront coding. In a larger aperture system, the additional wavelength bandwidth (alternately, the additional depth-of-focus) provided by the cubic phase and reconstruction becomes smaller. In other words, the amount of phase needs to be increased in a larger aperture system to provide the same benefit. Furthermore, the higher phase amount places tighter constraints on the system noise and makes the phase plate harder to manufacture. The trade-off between these parameters must be analyzed with the understanding that a high aperture system, like the microscope objective presented by Arnison et al. [20], may benefit from wavefront coding only if the other parameters are tightly controlled.

Aperture related assumptions were based upon a system with an approximately 100mm focal length. The first-order approach to scaling a system to a different focal length is to preserve constant surface slope of the optical elements. When a system is scaled leaving surface slopes constant, aberration contributions also change. Since the cubic phase mask must present the overwhelmingly dominant aberration in the system for wavefront coding to be effective, this method of scaling is effective in preserving the relationship between system aberrations. For a shorter focal length system, the aberration contributions are reduced. A scaled-down phase plate with the same surface slope also sees a smaller phase contribution.

Since the inherent aberrations of the scaled system have changed, the ideal contribution of the phase plate, in relation to the system aberrations, needs to be further examined. The ideal cubic phase contribution and the different geometry of the scaled system place new aperture constraints on the WFC system. Investigating the relationship between ideal phase amount and aperture constraints in a scaled-up or -down system presents an interesting avenue for future research. However, in any system, regardless of focal length, the conclusion stands that a larger aperture will place greater restrictions on other system parameters such as FOV and noise level.

7.3 Field of View

The isoplanatic patch is traditionally used to refer to a two-dimensional portion of the image, within which image quality is considered invariant. Typically, the isoplanatic patch is larger at small field angles around the optical axis and reduces in area toward the edge of the field due to the various field aberrations. Image quality within this region, while not nominally invariant, is restored to a consistent level after reconstruction. Since a cubic phase encoded system extends the axial depth of focus, we must consider a three-dimensional region, within which, the cubic phase encoded PSF is considered invariant. The paraxial focal length increases with wavelength, so the required axial depth of focus directly scales with bandwidth size.

Field of view in relation to cubic phase systems was not explicitly studied in this thesis, but a correlation can be drawn to the conclusions made with respect to bandwidth. Systems containing only axial chromatic aberration and no other aberrations are unaffected by field of view. This type of system, however, is unrealistic, as every system will see an increase of other aberrations if the field is increased large enough. Aberration contributions in physical systems are not generally limited to one aberration; usually many aberrations contribute to image blur in varying amounts. Furthermore, many aberrations increase with field, so we must consider their contributions when determining the benefit of cubic phase in systems with larger fields.

The pupil departure due to the monochromatic first and third-order wavefront aberrations are defined as follows:

$$\begin{aligned} \Delta W = \; & W_{111} && h\rho\cos(\theta) + \\ & W_{020} && \rho^2 + \\ & W_{040} && \rho^4 + \\ & W_{131} && h\rho^3\cos(\theta) + \\ & W_{222} && h^2\rho^2\cos^2(\theta) + \\ & W_{220} && h^2\rho^2 + \\ & W_{311} && h^3\rho\cos(\theta) \end{aligned}$$

Here, h is the normalized height at the image plane, ρ is the normalized radial pupil coordinate and θ is the pupil angular coordinate. W represents the wavefront aberration coefficient for the first-order aberrations tilt (W_{111}) and defocus (W_{020}) and third-order aberrations spherical (W_{040}), coma (W_{131}), astigmatism (W_{222}), field curvature (W_{220}) and distortion (W_{311}).

Let's begin by considering the impact of third-order field curvature on this three-dimensional isoplanatic region. Field curvature is a variation in focus with field height. When field curvature is present in a system, it essentially shifts the axial depth of focus for a particular field point so that it is no longer centered about the paraxial focal plane of the design wavelength (where we assume the design wavelength is chosen to be the center of the frequency bandwidth). This shift in focus means that bandwidth corrected in a cubic phase system gets shifted (typically toward the red end of the spectrum) as field height increases. For a single, full-field image, the correctable bandwidth then is decreased; or conversely, the amount of phase required to correct the original bandwidth increases.

Other third-order field aberrations coma, astigmatism, and distortion limit the isoplanatic region, but their contributions are not as straightforward. Coma and astigmatism destroy the symmetry of the cubic phase encoded PSF by shifting energy in various directions depending on the field location. Wavefront coding using cubic phase relies on having a similarly shaped PSF across the full field of view, so these aberrations reduce the ability of wavefront coding to reconstruct an image. Coma and astigmatism contributions are zero on-axis, so their presence simply limits the field angles that can be reconstructed. Monochromatic distortion is a variation in magnification with field location. Distortion doesn't actually blur the image, it merely moves the location of the image of a point from its paraxial location. Moderate amounts of monochromatic distortion can be easily removed using a computer algorithm. Distortion that varies with wavelength, however, is called transverse chromatic aberration and presents a greater challenge to wavefront coded systems. A variation in magnification with wavelength means that light a single object location focuses to different points based upon the wavelength. A camera with different color-sensitive pixels or one employing color filters can remove some of this transverse chromatic aberration during post processing. A monochromatic detector, on the other hand, is essentially stuck with this chromatic-based distortion. As with the other field-based aberrations, transverse chromatic aberration is zero on-axis and increases with field angle, so its presence in a wavefront coded system restricts the correctable image field.

7.4 WFC system performance with noise

Some optical systems require a high signal to noise ratio, while others may be able, or required, to operate in a much lower SNR regime. This inherent SNR requirement is caused by a few factors including available light level, exposure time (which may be limited due to camera or object motion), and aperture. Understanding the cutoff in SNR where wavefront coding becomes ineffective is critical, since in many systems, SNR is not considered until after a design form is chosen and developed. We established guidelines for an acceptable level of noise in a nominal image prior to reconstruction. We saw that systems with an initial SNR above 20 perform well with cubic phase and reconstruction, while systems with an SNR below 10 see an unacceptable image degradation as a result of image processing. SNR levels between 10 and 20 form an indeterminate area where certain applications, such as an edge detection system, may be able to tolerate the noise increase, while many will not. The cutoff SNR values were presented based upon our analysis of the experimental doublet and phase plate. These cutoff SNR values will change based upon the MTF curves of the coded image prior to processing; a system with MTF curves depressed to a larger extent will see a greater degradation of the processed image due to noise and will thus require a higher initial SNR.

Establishing a cutoff SNR places direct requirements on the type of detector used in a wavefront coded system. A camera with a dynamic range of 8 bits, with the brightest possible pixel value being 256, has a maximum SNR of 16 in the brightest areas of the image due to shot noise. A 9-bit detector has a maximum SNR of 22, while a 10-bit detector has a maximum SNR of 32. Reaching the maximum SNR assumes that the camera is exposed to saturation and other noise sources, such as read noise or dark current noise, are negligible. Darker areas of the image will have a much lower SNR, greatly increasing the effect of noise. Based upon the results of our experiment, a wavefront coded system would not perform well with an 8-bit camera outside the very brightest parts of the image.

The thought of using an 8-bit camera in an optical system may seem outdated, but it is actually a plausible problem. Consider the design of a digital camera used for amateur photography. The detector for such a camera likely has a much larger dynamic range than 8 bits. However, consumers often choose to save a compressed form of their images, instead of the raw data, to minimize file size. When a consumer saves their file in JPEG format, the data is usually compressed into an 8-bit file; the information from the extra bits is lost (JPEG has a few formats, but 8-bit is the most widely supported). In this scenario, a digital camera designed with wavefront coding would require larger images due to the inherent increase of noise. This may be an undesirable feature for some consumers and may limit the marketability of such a camera. Consequently, this information would be valuable to consider early in the design process before substantial resources are invested.

7.5 Rules of Thumb for Cubic Phase Systems

The following form a set of rules-of-thumb based upon the analysis and results of this research project for an optical system employing cubic phase wavefront coding.

- The desired correction bandwidth directly determines the required amount of cubic phase.

- Systems at F/10 and higher are likely good candidates for wavefront coding with cubic phase. Systems below F/5 require higher phase surface slopes and more tightly controlled system noise. Due to these restrictions, high aperture systems will likely be significantly restricted in the bandwidth that can be corrected.

- The field-of-view is restricted based upon the contributions of field-dependent aberrations. Large FOV systems require greater field aberration correction in the nominal system.

- The noise level must be understood prior to system design. At minimum, a 10-bit detector is required. Correspondingly, a minimum working SNR of 20 is necessary.

- The alignment difficulty of a cubic phase plate adds complexity to the manufacturing and testing of the optical system.

8 CONCLUSIONS

The first-order system parameters were largely analyzed independently, but the impact of each parameter on a system is not fully separable from the other parameters. The set of system parameters can be thought of in terms of an error budget; stressing the system in terms of one parameter places limitations on the other parameters when considering design complexity. For example, a system requiring a large field-of-view and a different system requiring a large aperture each attain a higher level of difficulty to design. However, a third system requiring both a large FOV and a large aperture is significantly more difficult to design than either of the first two systems.

The motivation of cubic phase systems was to relieve some of the imaging burden from the optics and place it, instead, on the electronics. We’ve shown that cubic phase will not be effective for all systems. However, there appears to be a set of systems which may benefit from this type of wavefront coding. Wavefront coding with cubic phase offers the possibility to simplify the optics of these systems; for example, replacing an achromatic doublet with a wavefront coded singlet. Systems, such as the triplet and double gauss lens follow a similar trend of increased complexity with carefully chosen materials for chromatic reduction. If field aberrations can be minimized for these more complex lenses, wavefront coding may again be an attractive option for a simplified electro-optical system.

9. REFERENCES

1. Cathey, W.T. and E.R. Dowski, *New paradigm for imaging systems.* Applied Optics, 2002. **41**(29): p. 6080-6092.
2. Chi, W.L. and N. George, *Electronic imaging using a logarithmic asphere.* Optics Letters, 2001. **26**(12): p. 875-877.
3. Chi, W.L. and N. George, *Computational imaging with the logarithmic asphere: theory.* Journal of the Optical Society of America a-Optics Image Science and Vision, 2003. **20**(12): p. 2260-2273.
4. Mikula, G., et al., *Diffractive elements for imaging with extended depth of focus.* Optical Engineering, 2005. **44**(5).
5. Ashok, A. and M.A. Neifeld, *Pseudorandom phase masks for superresolution imaging from subpixel shifting.* Applied Optics, 2007. **46**(12): p. 2256-2268.
6. Dowski, E.R. and W.T. Cathey, *EXTENDED DEPTH OF FIELD THROUGH WAVE-FRONT CODING.* Applied Optics, 1995. **34**(11): p. 1859-1866.
7. Mezouari, S. and A.R. Harvey, *Primary aberrations alleviated with phase pupil filters*, in *Novel Optical Systems Design and Optimization V*, J.M. Sasian and R.J. Koshel, Editors. 2002. p. 21-31.
8. Mezouari, S. and A.R. Harvey, *Combined amplitude and phase filters for increased tolerance to spherical aberration.* Journal of Modern Optics, 2003. **50**(14): p. 2213-2220.
9. Muyo, G. and A.R. Harvey, *Decomposition of the optical transfer function: wavefront coding imaging systems.* Optics Letters, 2005. **30**(20): p. 2715-2717.
10. Somayaji, M. and M.P. Christensen, *Frequency analysis of the wavefront-coding odd-symmetric quadratic phase mask.* Applied Optics, 2007. **46**(2): p. 216-226.
11. Zhang, W., et al., *Ray aberrations analysis for phase plates illuminated by off-axis collimated beams.* Optics Express, 2007. **15**(6): p. 3031-3046.
12. Zhang, W., et al., *Point spread function characteristics analysis of the wavefront coding system.* Optics Express, 2007. **15**(4): p. 1543-1552.
13. Stork, D.G. and M.D. Robinson, *Theoretical foundations for joint digital-optical analysis of electro-optical imaging systems.* Applied Optics, 2008. **47**(10): p. B64-B75.
14. Levoy, M., et al., *Light field microscopy.* Acm Transactions on Graphics, 2006. **25**(3): p. 924-934.
15. Veeraraghavan, A., et al., *Dappled photography: Mask enhanced cameras for heterodyned light fields and coded aperture refocusing.* Acm Transactions on Graphics, 2007. **26**(3).
16. Lee, S.-H., N.-C. Park, and Y.-P. Park, *Breaking diffraction limit of a small f-number compact camera using wavefront coding.* Optics Express, 2008. **16**(18): p. 13569-13578.
17. Siviloglou, G., et al., *Airy beams: a new class of optical waves.* Optics & Photonics News, 2008. **19**(12): p. 21-21.
18. Zhang, R., et al., *Analyzing wavelength behavior of a cubic phase mask imaging system based on modulation transfer function.* Optics Communications, 2012. **285**(6): p. 1082-1086.
19. Heide, F., et al., *High-Quality Computational Imaging through Simple Lenses.* Acm Transactions on Graphics, 2013. **32**(5).
20. Arnison, M., et al., *Wavefront coding fluorescence microscopy using high aperture lenses*, in *Optical Imaging and Microscopy: Techniques and Advanced Systems*. 2003.

21. Brady, G., *Application of Phase Retrieval to the Measurement of Optical Surfaces and Wavefronts*, 2008, University of Rochester.
22. Goodman, J., *Introduction to Fourier Optics*. Physical and Quantum Electronics Series. 2005: McGraw-Hill.
23. Burns, P., *sfrmat3: SFR evaluation for digital cameras and scanners*.
24. Iso 12233:2000(e), p.-e.s.-p.c.-r.m.
25. Reichenbach, S.E., S.K. Park, and R. Narayanswamy, *CHARACTERIZING DIGITAL IMAGE ACQUISITION DEVICES.* Optical Engineering, 1991. **30**(2): p. 170-177.
26. Howell, S., *Handbook of CCD Astronomy*. 2000: Cambridge University Press.
27. Hopkinson, G., *A guide to the use and calibration of detector array equipment*. 2004: SPIE Press.
28. Ekstrom, M.P., *Digital Image Processing Techniques (Computational Techniques)*. 1984.: Academic Press.
29. Somayaji, M., V.R. Bhakta, and M.P. Christensen, *Experimental evidence of the theoretical spatial frequency response of cubic phase mask wavefront coding imaging systems.* Optics Express, 2012. **20**(2): p. 1878-1895.
30. *Scientific Volume Imaging. Signal-to-noise ratio,* . 2013; Available from: http://www.svi.nl/SignalToNoiseRatio.
31. Lipson, A., S. Lipson, and H. Lipson, *Optical Physics*. 2010: Cambridge University Press.

[Blank page following section.]

APPENDIX A: MATLAB CODE FOR EXPERIMENTAL RECONSTRUCTION

Here is a sample code for reconstruction of experimentally taken images using the experimentally collected PSF.

```
%% WC_ImageRecon
% Using experimental images with experimentally measured PSF
%
% Rob Boye, 29-November-2012
% Modified: David Scrymgeour 9-10-13
% Modified: 9-11 incorporating Rob's new deconvolution routine
% Modified: 9-17 automate collection of MTF curve from line pairs
%
% Using experimental images AND experimental PSF collected ~09-10-2013

%% Basic parameters and inputs
clear
close all
clc
fig = 0;

time = clock;

% Parameters for deconvolution
threshold = 0.001; % Threshold for inverse filter operation
gamma=1.0;     % Parameter of Wiener filter used during removal of singularities (and values
lower than threshold)
smooth = 11;    %smoothing kernel of OTF
PSF_rot = 0;    % If phase plate was rotated, it can be adjusted here - in deg

%cross sections to compare between images
Bar(1,:) = [349,610,900,900];  %0,1 Bottom middle
Bar(2,:) = [134,354,161,161];  %0,2 Left row, 1 (top)
Bar(3,:) = [117,310,391,391];  %0,3 Left row, 2
Bar(4,:) = [93,269,586,586];   %0,4 Left row, 3
Bar(5,:) = [72,251,754,754];   %0,5 Left row, 4
Bar(6,:) = [60,210,900,900];   %0,6 Left row, 5 (bottom)
Bar(7,:) = [565,697,143,143];  %1,1 Right row, 1 (top)
Bar(8,:) = [592,709,268,268];  %1,2 Right row, 2
Bar(9,:) = [610,721,379,379];  %1,3 Right row, 3
Bar(10,:)= [631,733,478,478];  %1,4 Right row, 4
Bar(11,:)= [652,745,568,568];  %1,5 Right row, 5
Bar(12,:)= [667,750,643,643];  %1,6 Right row, 6 (bottom)
Bar(13,:)= [464,535,611,611];  %2,1 Middle right, (bottom)
Bar(14,:)= [418,473,439,439];  %2,2 Middle left, 1 (top)
Bar(15,:)= [411,463,498,498];  %2,3 Middle left, 2
Bar(16,:)= [407,454,545,545];  %2,4 Middle left, 3
Bar(17,:)= [401,445,588,588];  %2,5 Middle left, 4
Bar(18,:)= [398,437,628,628];  %2,6 Middle left, 5 (bottom)
Bar(19,:)= [527,561,431,431];  %3,1 Middle right, 1 (top)
Bar(20,:)= [535,563,464,464];  %3,2 Middle right, 2
Bar(21,:)= [542,566,491,491];  %3,3 Middle right, 3
Bar(22,:)= [547,568,516,516];  %3,4 Middle right, 4
Bar(23,:)= [551,571,537,537];  %3,5 Middle right, 5
Bar(24,:)= [555,572,556,556];  %3,6 Middle right, 6
Bar(25,:)= [494,503 ,505,505];  %4,1 too blurry!
Bar(26,:)= [488,498 ,520,520];  %4,2 too blurry!
Bar(27,:)= [486,496 ,532,532];  %4,3 too blurry!
Bar(28,:)= [485,494,543,543];  %4,4 too blurry!
Bar(29,:)= [485,493,553,553];  %4,5 too blurry!
bn=7;

%from 1951 USAF resolution target - data in (line pairs/mm)
linepairs =
[0.25,0.28,0.315,0.353,0.397,0.445,0.5,0.561,0.63,0.707,0.793,0.891,1,1.12,1.26,1.41,1.59,1.78,2,
2.24,2.52,2.83,3.17,3.56, 4,4.49,5.04,5.66,6.35,7.13];
```

```
%plotting stuff
plotpsf = 0;  %1 to plot the uncorrected PSF
plotproc = 0; %1 to plot the processed PSF
crossplot = 0;  %1 to plot cross sections across linepairs
zoom = 0;  %1 to zoom in, otherwise plot entire figure
corner = [400,376];
zoomset = [corner(1),corner(1)+250,corner(2),corner(2)+250];  %x1,x2,y1,y2

%Image sets input here
qq = 1;
if qq == 1  %f10, 500nm
    lambda = '500 nm';
    aperture = '8 mm';
    focus = 'best focus';
    PSF_lambda = '500 nm';
    PSF_focus = 'best focus';
    conv_pre = '\\snl\Mesa\Users\Boye\Wavefront Coding\David Images\Waveplate Series 09-
09\Conv_500_-30C_22s';
    wc_pre = '\\snl\Mesa\Users\Boye\Wavefront Coding\David Images\Waveplate Series 09-09\WC_500_-
30C_25s';
    PSF_image = fitsread('\\snl\Mesa\Users\Boye\Wavefront Coding\David Images\PSF Images 09-
05\500_psf_bestfocus.fit','Primary'); %psf image

    conv_dark_image = fitsread([conv_pre,'_dark.fit'],'Primary');
    conv_flat_image = fitsread([conv_pre,'_bright.fit'],'Primary');
    conv_image = fitsread([conv_pre,'.fit'],'Primary');  %conventional

    wc_image = fitsread([wc_pre,'.fit'],'Primary');  %waveplate
    wc_dark_image = fitsread([wc_pre,'_dark.fit'],'Primary');
    wc_flat_image = fitsread([wc_pre,'_bright.fit'],'Primary');

end

%% Reading in & correcting conventional image
conv_image = conv_image - conv_dark_image;
conv_image = conv_image ./ (conv_flat_image/max(max(conv_flat_image)));
image_max = max(max(conv_image));
image_min = min(min(conv_image));
conv_image = (255*(conv_image-image_min)/(image_max-image_min));  %makes min 0 max 255

fig = fig + 1;
figure(fig)
if zoom == 1
    imagesc( conv_image(zoomset(1):zoomset(2),zoomset(3):zoomset(4)) ); hold on
else
    imagesc(conv_image); hold on
    plot3([Bar(bn,1),Bar(bn,2)],[Bar(bn,3),Bar(bn,4)],[100,100],'r');
end
colormap(gray(256))
axis equal tight
title(['Conventional image (',lambda,' ',aperture,' ',focus,')']);

% Reading in & correcting wavefront coded image
wc_image = wc_image - wc_dark_image;  %dark image correction
wc_image = wc_image ./ (wc_flat_image/max(max(wc_flat_image)));  %bright image correction
image_max = max(max(wc_image));
image_min = min(min(wc_image));
wc_image = (255*(wc_image-image_min)/(image_max-image_min)); %makes data min 0 max 255

%take care of slight offsets between two images so they align
conv_p = [388,271];  %location bottom left of square block
wc_p = [410,249];    %location bottom left of square block
offx = conv_p(1) - wc_p(1);
offy = conv_p(2) - wc_p(2);

%apodize the WC image to deal with tiling of FFT
[X,Y] = meshgrid(-511:512);
superG_1d = exp(-((X(1,:)).^2/2/350^2).^12);
superG_2d = superG_1d'*superG_1d;
wc_image = wc_image.*superG_2d;
```

```
%plot wavefront coded image
fig = fig + 1;
figure(fig)
if zoom==1
    imagesc( wc_image(zoomset(1)+offx:zoomset(2)+offx,zoomset(3)+offy:zoomset(4)+offy) ); hold on
else
    imagesc( wc_image ); hold on;
    plot3([Bar(bn,1)-offx,Bar(bn,2)-offx],[Bar(bn,3)-offy,Bar(bn,4)-offy],[100,100],'g');
end
colormap(gray(256))
axis equal tight
title(['Wavefront coded image (',lambda,' ',aperture,' ',focus,') apodized']);

% Plotting PSF image
if plotpsf == 1
    fig = fig + 1;
    figure(fig)
    imagesc(PSF_image)
    colormap(jet(256))
    axis equal tight
    title(['PSF (',PSF_lambda,' ',aperture,' ',PSF_focus,')']);
end

% Reading in PSF image
% Expand the PSF to a full 1024x1024 - collected at 200x200
% Drop zoomed in version into full field of average value pixels
[x,y] = find(PSF_image == max(max(PSF_image)));  %finds center of PSF
PSF_background = mean(mean(PSF_image(:))); %background value of PSF
temp = PSF_background .* ones(1024,1024);  %Makes background mean value of image
temp(512-x:711-x,512-y:711-y) = PSF_image;  %places PSF in middle of field
PSF_image = temp;
PSF_image = (255*(PSF_image-min(PSF_image(:)))/(max(PSF_image(:))-min(PSF_image(:))));
PSF_image = PSF_image/sum(sum(PSF_image));  %divide by sum of pixels - critical!!

%% Rotating PSF to match phase plate from QED - CCW rotation
N = 1024;
theta = PSF_rot*pi/180;  %now in radians
center_y = 512;
center_x = 512;
for index1 = 1:N
    for index2 = 1:N
        x_coord = round((index1-center_x)*cos(theta) - (index2-center_y)*sin(theta) + center_x);
        y_coord = round((index1-center_x)*sin(theta) + (index2-center_y)*cos(theta) + center_y);
        if (x_coord > N || y_coord > N || x_coord < 1 || y_coord < 1)
            PSF_rotate(index1,index2) = 0;
        else
            PSF_rotate(index1,index2) = PSF_image(x_coord,y_coord);
        end
    end
end
PSF_image = PSF_rotate;

if plotproc == 1
    fig = fig + 1;
    figure(fig)
    imagesc(PSF_image(412:612,412:612))
    colormap(jet(256))
    axis equal
    title(['Processed PSF (',PSF_lambda,' ',aperture,' ',PSF_focus,')']);
end

%% Reconstructing image

%collect contrast for MTF calculations & noise data
conv_d = conv_image(116:254,409:532);  %in dark square
conv_b = conv_image(670:790,409:532);  %in bright square
conv_c0 = (mean(conv_b(:)) - mean(conv_d(:)) ) / (mean(conv_b(:)) + mean(conv_d(:)) );
conv_noise_d = [mean(conv_d(:)), std(conv_d(:)), mean(conv_d(:))/std(conv_d(:))];  %noise in
conventional dark
```

```
conv_noise_b = [mean(conv_b(:)), std(conv_b(:)), mean(conv_b(:))/std(conv_b(:))];  %noise in conventional bright

wc_d = wc_image(100:224,427:547);  %in dark square
wc_b = wc_image(650:770,427:547);  %in bright square
wc_c0 = (mean(wc_b(:)) - mean(wc_d(:)) ) / (mean(wc_b(:)) + mean(wc_d(:)) );
wc_noise_d = [mean(wc_d(:)), std(wc_d(:)), mean(wc_d(:))/std(wc_d(:))]; %noise in WC dark
wc_noise_b = [mean(wc_b(:)), std(wc_b(:)), mean(wc_b(:))/std(wc_b(:))]; %noise in WC bright

%Begin reconstruction - first FFT the PSF
filt_OTF = fftshift(PSF_image);
filt_OTF = fft2(filt_OTF);
filt_OTF = fftshift(filt_OTF);

WC_OTF_nonsing = (filt_OTF).*(abs(filt_OTF)>threshold) + 1/gamma.*(abs(filt_OTF)<=threshold);
InvFilt = (1./WC_OTF_nonsing);

%smooth inverse filter using smoothing kernel
filt_smooth = ones(smooth,smooth);
filt_smooth = filt_smooth/sum(sum(filt_smooth));
InvFilt = convn(InvFilt,filt_smooth,'same');

%fft the wc image
output_image_fft = fftshift(wc_image(:,:));
output_image_fft = fft2(output_image_fft);
output_image_fft = (fftshift(output_image_fft));

%reconstruct the wc image
deblur_fft = output_image_fft.*InvFilt;
deblur_image = fftshift(deblur_fft);
deblur_image = ifft2(deblur_image);
deblur_image = abs(fftshift(deblur_image));

image_max = max(max(deblur_image));
image_min = min(min(deblur_image));
deblur_image = (255*(deblur_image-image_min)/(image_max-image_min));  %normalize

%plot up reconstructed image
fig = fig + 1;
figure(fig)
if zoom == 1
    imagesc( deblur_image(zoomset(1)+offx:zoomset(2)+offx,zoomset(3)+offy:zoomset(4)+offy) );
else
    image(deblur_image); hold on
    plot3([Bar(bn,1)-offx,Bar(bn,2)-offx],[Bar(bn,3)-offy,Bar(bn,4)-offy],[100,100],'b');
end
axis equal tight
colormap(gray(256));
title(['Reconstructed image (',lambda,' ',aperture,' ',focus,')']);

disp(' ')
disp('RC Image details');
fprintf('min/max [ %.2f , %.2f] mean %.2f',min(deblur_image(:)),max(deblur_image(:)),mean(deblur_image(:)));
disp(' ');

%contrast for MTF calculations============================================
%collect contrast for all the images
conv_d = conv_image(116:254,409:532);  %in dark square
conv_b = conv_image(670:790,409:532);  %in bright square
conv_c0 = (mean(conv_b(:)) - mean(conv_d(:)) ) / (mean(conv_b(:)) + mean(conv_d(:)) );

wc_d = wc_image(100:224,427:547);  %in dark square
wc_b = wc_image(650:770,427:547);  %in bright square
wc_c0 = (mean(wc_b(:)) - mean(wc_d(:)) ) / (mean(wc_b(:)) + mean(wc_d(:)) );

rc_image = deblur_image;
rc_d = rc_image(100:224,427:547);  %in dark square
rc_b = rc_image(650:770,427:547);  %in bright square
rc_c0 = (mean(rc_b(:)) - mean(rc_d(:)) ) / (mean(rc_b(:)) + mean(rc_d(:)) );
```

```
disp(' ');
fprintf('Contrast in Conv image bright/dark [ %.2f , %.2f ], value %.2f \n',mean(conv_d(:)),
mean(conv_b(:)), conv_c0);
fprintf('Contrast in WC image bright/dark [ %.2f , %.2f ], value %.2f \n',mean(wc_d(:)),
mean(wc_b(:)), wc_c0);
fprintf('Contrast in RC image bright/dark [ %.2f , %.2f ], value %.2f \n',mean(rc_d(:)),
mean(rc_b(:)), rc_c0);
disp(' ');

%Extract cross sections to pull out MTF information
for qq = 1:29

    bn = qq;
    xv = [1:(Bar(bn,2)-Bar(bn,1))+1];
    conv_cross = conv_image(Bar(bn,3),Bar(bn,1):Bar(bn,2));
    wc_cross = wc_image(Bar(bn,3)+offx,Bar(bn,1)+offy:Bar(bn,2)+offy);
    rc_cross = rc_image(Bar(bn,3)+offx,Bar(bn,1)+offy:Bar(bn,2)+offy);

    %find edges of data of interest ==================================
    %find thresholds to capture the data of interest
    conv_thresh = min(conv_cross) + 0.15*(max(conv_cross)-min(conv_cross));
    wc_thresh =   min(wc_cross) + 0.15*(max(wc_cross)-min(wc_cross));
    rc_thresh =   min(rc_cross) + 0.15*(max(rc_cross)-min(rc_cross));

    %consider only values between first & last dip (ignore the left & right edge)
    a = find(conv_cross < conv_thresh);
    conv_edge = [a(1), a(length(a))];
    clear a
    a = find(wc_cross < wc_thresh);
    wc_edge = [a(1), a(length(a))];
    clear a
    a = find(rc_cross < rc_thresh);
    rc_edge = [a(1), a(length(a))];
    clear a

    %Now calculate an average value for top and bottom ====================
    %only care about data within conv_edge
    xv_conv = xv(conv_edge(1):conv_edge(2));
    conv_cross_sub = conv_cross(conv_edge(1):conv_edge(2));
    xv_wc = xv(wc_edge(1):wc_edge(2));
    wc_cross_sub = wc_cross(wc_edge(1):wc_edge(2));
    xv_rc = xv(rc_edge(1):rc_edge(2));
    rc_cross_sub = rc_cross(rc_edge(1):rc_edge(2));

    %Average values above or below these thresholds
    conv_thresh_lo = min(conv_cross_sub) + 0.1*(max(conv_cross_sub)-min(conv_cross_sub));
    conv_thresh_hi = min(conv_cross_sub) + 0.85*(max(conv_cross_sub)-min(conv_cross_sub));

    wc_thresh_lo = min(wc_cross_sub) + 0.1*(max(wc_cross_sub)-min(wc_cross_sub));
    wc_thresh_hi = min(wc_cross_sub) + 0.85*(max(wc_cross_sub)-min(wc_cross_sub));

    rc_thresh_lo = min(rc_cross_sub) + 0.1*(max(rc_cross_sub)-min(rc_cross_sub));
    rc_thresh_hi = min(rc_cross_sub) + 0.6*(max(rc_cross_sub)-min(rc_cross_sub));

    %find contrast values above and below thresholds
    a1 = find( conv_cross_sub > conv_thresh_hi) + conv_edge(1) -1;  %indexed to full data
    a2 = find( conv_cross_sub < conv_thresh_lo) + conv_edge(1) -1;
    Contrast_conv_hi(qq) = mean(conv_cross(a1));
    Contrast_conv_lo(qq) = mean(conv_cross(a2));
    Contrast_conv(qq) = (Contrast_conv_hi(qq)-Contrast_conv_lo(qq)) ./
(Contrast_conv_hi(qq)+Contrast_conv_lo(qq));
    MTF_conv(qq) = Contrast_conv(qq) / conv_c0;

    a3 = find( wc_cross_sub > wc_thresh_hi) + wc_edge(1) -1;  %indexed to full data
    a4 = find( wc_cross_sub < wc_thresh_lo) + wc_edge(1) -1;
    Contrast_wc_hi(qq) = mean(wc_cross(a3));
    Contrast_wc_lo(qq) = mean(wc_cross(a4));
    Contrast_wc(qq) = (Contrast_wc_hi(qq)-Contrast_wc_lo(qq)) ./
(Contrast_wc_hi(qq)+Contrast_wc_lo(qq));
    MTF_wc(qq) = Contrast_wc(qq) / wc_c0;
```

```
    a5 = find( rc_cross_sub > rc_thresh_hi) + rc_edge(1) -1;  %indexed to full data
    a6 = find( rc_cross_sub < rc_thresh_lo) + rc_edge(1) -1;
    Contrast_rc_hi(qq) = mean(rc_cross(a5));
    Contrast_rc_lo(qq) = mean(rc_cross(a6));
    Contrast_rc(qq) = (Contrast_rc_hi(qq)-Contrast_rc_lo(qq)) ./
(Contrast_rc_hi(qq)+Contrast_rc_lo(qq));
    MTF_rc(qq) = Contrast_rc(qq) / rc_c0;

    %Cross sections
    if crossplot == 1
    fig = fig + 1;
    figure(fig)
    plot(xv, conv_cross, '-or', xv, wc_cross, '-ob', xv, rc_cross, '-og'); hold on;
    plot(xv_wc, Contrast_wc_hi(qq).*ones(size(xv_wc)),':b',xv_wc,
Contrast_wc_lo(qq).*ones(size(xv_wc)),':b');
    plot(xv_conv, Contrast_conv_hi(qq).*ones(size(xv_conv)),':r',xv_conv,
Contrast_conv_lo(qq).*ones(size(xv_conv)),':r');
    plot(xv_rc, Contrast_rc_hi(qq).*ones(size(xv_rc)),':g',xv_rc,
Contrast_rc_lo(qq).*ones(size(xv_rc)),':g');
    ylabel('Intensity (black = 0)');
    axis square
    Ctext = ['Conv [ ',num2str(Contrast_conv_lo(qq),'%.2f'), ' ,
',num2str(Contrast_conv_hi(qq),'%.2f'),' ] MTF = ',num2str(MTF_conv(qq),'%.2f')];
    wctext= ['WC   [ ',num2str(Contrast_wc_lo(qq),'%.2f'), ' ,
',num2str(Contrast_wc_hi(qq),'%.2f'),' ] MTF = ',num2str(MTF_wc(qq),'%.2f')];
    rctext= ['Recon[ ',num2str(Contrast_rc_lo(qq),'%.2f'), ' ,
',num2str(Contrast_rc_hi(qq),'%.2f'),' ] MTF = ',num2str(MTF_rc(qq),'%.2f'),' Co ',num2str(rc_c0,
'%.2f')];
    legend(Ctext,wctext,rctext,'location','NW');
    legend boxoff
    axis([0,length(wc_cross),0,300]);
    title(['Cross section #',num2str(qq)]);
    end

end

linepairs = linepairs(1:qq);

fig=fig+1;
figure(fig)
plot(linepairs, MTF_conv, 'or', linepairs, MTF_wc, 'bo', linepairs, MTF_rc, 'go');
ylabel('Contrast');
xlabel('Line pair/mm');
axis square
legend('Conventional', 'Wavefront Coded','Reconstructed','location','NE');
legend boxoff
%title(['WC - Cross section #',num2str(qq)]);

%plot up contrast of WC image not the MTF
fig=fig+1;
figure(fig)
plot(linepairs, MTF_conv, 'or', linepairs, MTF_wc, 'bo', linepairs, MTF_rc.*rc_c0, 'go');
ylabel('Contrast');
xlabel('Line pair/mm');
axis square
legend('Conventional', 'Wavefront Coded','Reconstructed - no /c0','location','NE');
legend boxoff
%title(['WC - Cross section #',num2str(qq)]);

elapsed = etime(clock, time);
fprintf('Elapsed time for run %.2f sec \n',elapsed);

tile
```

Distribution

1	MS1082	Rob Boye	1728
1	MS1082	David Scrymgeour	1728
1	MS0359	D. Chavez, LDRD Office	1911
1	MS0406	Ronald Baker	5783
1	MS0899	Technical Library	9536 (electronic copy)

Sandia National Laboratories